Development of a Hadron Blind Detector for the J-PARC E16 Experiment

Koki Kanno *

March 1, 2013

Abstract

A Hadron Blind Detector (HBD) has been developed for the J-PARC E16 experiment. The E16 experiment aims to measure mass spectra of vector mesons in nuclei using an electron decay mode. The experiment requires large acceptance electron identification detector to have enormous huge statistics. The HBD is the best candidate for an electron identification detector, since it can cover huge acceptance due to its mirror-less and window-less structure. The HBD is a mirror-less and window-less Čerenkov detector operated with pure CF_4 and used for electron identification. It has a 50 cm radiator directly coupled to a readout element consisting of a triple Gas Electron Multiplier (GEM) stack, with CsI photocathode evaporated on the top surface of the top GEM and pad readout at the bottom of the stack. The HBD was originally developed, constructed and operated for the PHENIX experiment at RHIC and we have improved the HBD for the E16 experiment. We have performed several developments and test in a laboratory to have good detector components, such as CsI photocathode, GEM foils and high transmission gas radiator. Based on results of laboratory tests, we construct a prototype HBD. The prototype HBD is tested at J-PARC K1.1BR beamline. 7 photoelectrons are observed and a pion rejection factor of 100 is achieved with an electron detection efficiency of 70 %. These values satisfy requirements of the E16 experiment. This thesis gives an account of the development and performance of the HBD.

*Department of Physics, Graduate School of Science, University of Tokyo

Contents

1 Introduction

Quantum chromodynamics (QCD), which is the color SU(3) gauge theory of quarks and gluons is now established as a fundamental theory of strong interactions. The Lagrangian density of QCD is given by

$$\mathcal{L} = \sum_q (\bar{q}_L i \not{D} q_L + \bar{q}_R i \not{D} q_R) - \frac{1}{4} G^{\alpha}_{\mu\nu} G^{\mu\nu}_{\alpha} + \sum_q (\bar{q}_L m q_R + \bar{q}_R m q_L) \tag{1}$$

where $q = (u, d, s)$ with the mass matrix m = diag(m_u, m_d, m_s). In contrast to such a simple form, QCD shows various phenomena due to the running coupling constant. The running coupling constant $g(\kappa)$ is defined as an effective coupling strength among quarks and gluons at the energy scale κ. The coupling constant $g(\kappa)$ becomes small as κ increases, which is called the asymptotic freedom [1]. The asymptotic freedom nature of QCD can be clearly seen in the two-loop perturbation theory

$$\alpha_s^{(2)}(z) = \frac{1}{\beta_0 \ln z}\left[1 - \frac{\beta_1}{\beta_0 2}\frac{\ln(\ln z)}{\ln z}\right] \tag{2}$$

where $\alpha_s^{(2)}(z) \equiv \frac{g^2(\kappa)}{4\pi}$, $z = \kappa^2/\Lambda^2$, $\beta_0 = (11 - \frac{2}{3}N_f)/(4\pi)^2$, $\beta_1 = (102 - \frac{38}{3}N_f/(4\pi)^4)$, N_f is the number of flavors and Λ is called the QCD scale parameter.

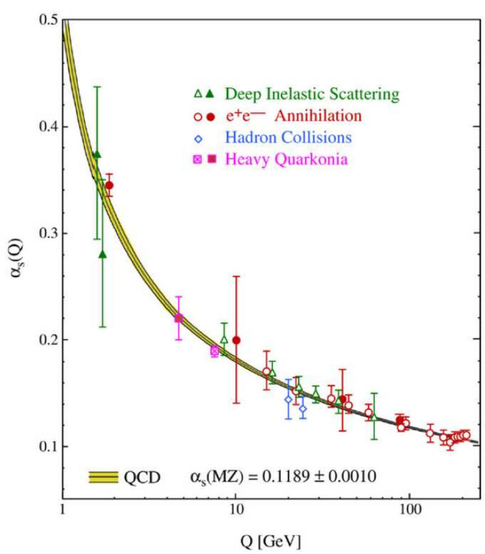

Fig. 1: Coupling constant of QCD as a function of energy scale [2]. Many experiments are in good agreement with each other.

This equation and Fig. 1 indicate that at high energy region the interaction between quarks and gluons is weak, however at low energy scale $\kappa \sim \Lambda \sim 200$MeV, the running coupling constant increases and become strong. This is the typical energy scale where various non-perturbative phenomena, such as the confinement [3] and the dynamical breaking of the chiral symmetry [4] [5] occur. At low energy, QCD is in the confined phase where chiral symmetry is spontaneously broken while at high energy quarks and gluons form a correlated plasma in which chiral symmetry is restored. The various phases of QCD are characterized by order parameters of the chiral symmetry. These order parameters are vacuum expectation values of certain gauge invariant products of quark and gluon operators and are usually referred to as condensates. The most prominent ones are the quark condensate $\langle \bar{q}q \rangle$ and the gluon condensate $\langle G_{\mu\nu}G^{\mu\nu} \rangle$. The quark condensate $\langle \bar{q}q \rangle$ is a well-known order parameter of chiral symmetry breaking: It is non-zero in the chiral symmetry broken phase and vanishes (for mass less quark) in the chirally symmetric phase. Temperature and density dependence of the quark condensate is shown in Fig. 2. As temperature (density) increases,

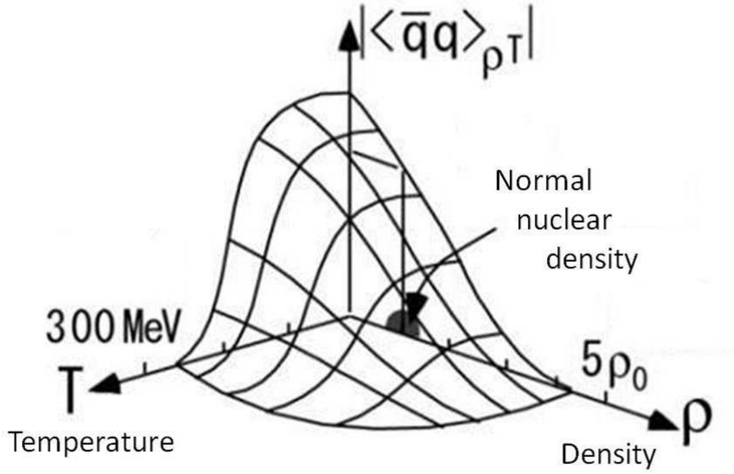

Fig. 2: QCD phase diagram. An order parameter of chiral symmetry $\langle \bar{q}q \rangle$ is drawn as a function of density and temperature.

the absolute value of $\langle \bar{q}q \rangle$ decreases and finally goes to zero at a critical temperature (density). The chiral symmetry is expected to restore at finite temperature and/or density. Unfortunately, $\langle \bar{q}q \rangle$ itself is not an observable, therefore other observables which reflect the $\langle \bar{q}q \rangle$ value should be studied. The spectral properties of hadrons like the mass and the decay width are good candidates. Measurements of hadron properties in hot/dense matter are considered as a powerful and unique probe to the chiral symmetry restoration. We are especially interested in the origin of hadronic mass which related to the chiral symmetry. There are numerous theoretical attempts to the hadron property in the medium [6] [7] [8] and some experiments already detected the modification of the hadron spectra in hot/dense matter [9–14].

As an example, the results of E325, which was carried at KEK 12 GeV Proton Synchrotron, are shown in Fig. 3 and Fig. 4. The invariant mass spectra of e^+e^- pairs produced in a nuclear reaction, p+A $\rightarrow$ X+$\rho/\omega/\phi$, was investigated. Two types of targets, carbon and copper, were used. Mass spectra with different $\beta\gamma$ range for C and Cu are shown in Fig. 3. The spectra are fitted with resonance shape of $\phi \rightarrow e^+e^-$ and a quadratic background. Both C and Cu data with $\beta\gamma > 1.25$ are well reproduced by the fit, however Cu data with $\beta\gamma < 1.25$ have significant excess on low-mass side of the peak. Mass spectrum of wider range for C and Cu target is shown in Fig. 4. Combinatorial background are already subtracted. The shape of combinatorial background is estimated with the event-mixing method. Assuming the density dependence of ρ/ω mass as $m(\rho)/m(0) = 1 - k_1(\rho/\rho_0)$, k_1 is estimated to be $\sim 0.092 \pm 0.002$. However, the origin of modification is not clarified yet and there are many explanation unrelated to the chiral symmetry. To investigate this problem, J-PARC E16 experiment are proposed. The main aim of E16 is a measurement of e^+e^- pair from the p+A reaction to investigate the chiral symmetry around normal nuclear matter density with higher statistics and improved mass resolution. To achieve the aim of E16 experiment, we need to construct a new spectrometer using new technologies. This thesis explains a part of the spectrometer for electron identification.

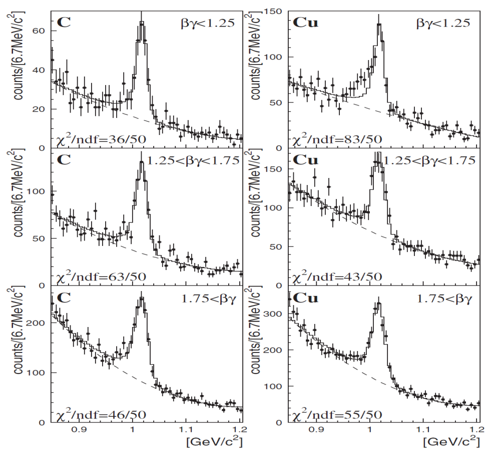

Fig. 3: A result from E325. These mass spectra are obtained by reconstructing the invariant mass of ϕ in-medium. Clear excess is observed for slowly moving ϕ in Cu target [11].

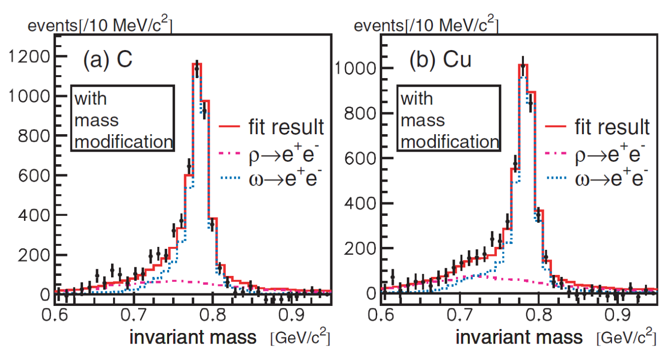

Fig. 4: A result from E325. The mass spectra of wide mass range for C and Cu targets.

2 J-PARC E16 Experiment

2.1 Overview

The J-PARC E16 experiment measures precise mass spectra of light vector mesons in nuclei with high statistics to investigate a restoration of the chiral symmetry at finite density. In E16 experiment, light vector mesons are generated by the 30-GeV proton induced reaction in target nucleus. Meson mass spectra are reconstructed by using e^+e^- pair decay channel. Slowly moving mesons decay in the target nucleus and will show the mass modification in the spectra. The branching ratio of this channel is relatively small (order of 10^{-4} to 10^{-5}), however this leptonic channel doesn't suffer from final state interactions. Consequently, clear mass spectra will be obtained.
The high statistics capability in the E16 experiment enable us to use various targets with reasonable statistics. It means we can measure the target mass dependence of meson mass spectra. Large nucleus such as Pb enhances the possibility of vector meson's decaying inside, which is very important for the measurement of mass spectrum in the nuclear matter. A radiation length is proportional to A/Z^2 and increase rapidly as nucleus is larger. Thus very thin target is required for measurement of large nucleus to reduce radiation tail. This was given up in the KEK-PS E325 due to the statistical limitation. However, the E16 experiment can use these large nucleus targets due to its high statistics. A hydrocarbon target and a carbon one are planned to be bombarded by primary proton beam as well as heavier targets. Meson mass spectra in proton-on-proton collisions will be obtained by subtracting the contribution of carbon nuclei target from the hydrocarbon target data. This proton-on-proton data can be used to subtract the non-modified mass spectrum peak in the spectrum of heavier target nuclei. This was given up in the KEK-PS E325 due to the statistical limitation. The expected spectrum of the ϕ meson is shown in Fig. 5. The statistics is expected to be improved from KEK-PS E325 by following ways.

1. 10 times higher beam intensity
2. 2 times larger cross section
3. 5 times larger acceptance

The first and the second factor require a new beam line. The third factor requires a new spectrometer.

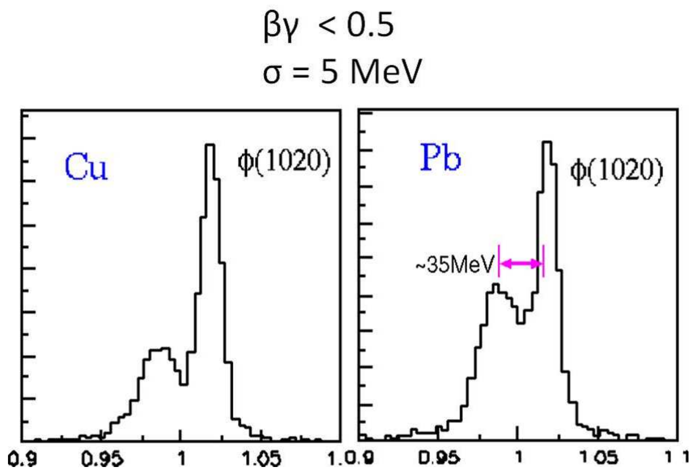

Fig. 5: Expected spectra of ϕ meson in Copper and Lead under the assumption of 5 MeV mass resolution. These spectra show the clear double-peak. The lighter mass peak reflects the restoration of the chiral symmetry and the peak around 1020 MeV is mass of ϕ meson in vacuum. The mass peak of 1020 MeV can be obtained by subtracting the contribution of carbon nuclei target from the hydrocarbon target data.

2.2 Beam Line

E16 experiment will use a high-momentum beam line. Primary proton of 30-GeV is delivered to the beam line from J-PARC main ring. The beam intensity of 10^{10} per spill and the spill length of 2 sec are required. The spectrometer is placed at the final focus point of the beam line as shown in Fig. 6.

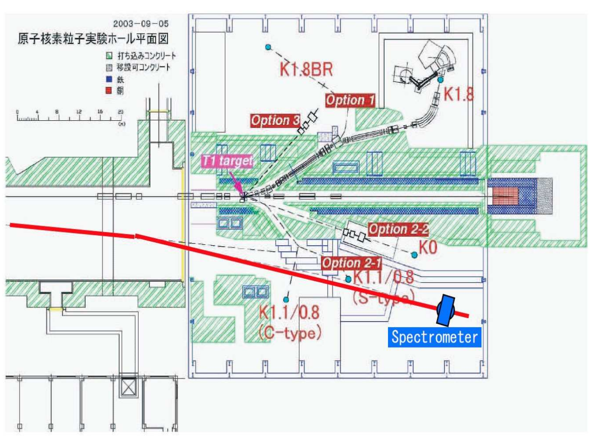

Fig. 6: The schematic view of High-Momentum Beam Line in J-PARC hadron hall. Our new spectrometer are placed at the final focus point of the beam line.

	nuclei	interaction length (%)	radiation length (%)	thickness (μm)
E325	C	0.21	0.43	81
	Cu	0.054	0.57	81
E16	C	0.05	0.1	200
	CH_2	0.05	0.1	400
	Cu	0.05	0.5	80
	Pb	0.01	0.3	20

Table 1: Nucleus targets of E325 and E16.

2.3 Spectrometer Design

The spectrometer has following basic concepts.

- using thin target shown in Table 1 ($\sim$0.1% interaction length) to reduce radiation tail. Energy loss of electrons in targets can make a tail in low mass region of vector mesons.
- large acceptance covering the backward in CM system to detect the slowly moving mesons.
- high intensity tolerance. Beam intensity of high-momentum beam line is 10^{10} per spill and target thickness is about 0.1% interaction length, so the interaction rate is approximately 10^7 Hz.

To achieve these concepts, we need a sophisticated spectrometer using new technologies. These new technologies are almost based on Gas Electron Multiplier (GEM) [15]. Our new spectrometer has large geometrical acceptance and are divided into 26 modules. The vertical acceptance is $\pm 45°$ and the horizontal acceptance is $\pm 135°$. The very forward region of $0 \sim \pm 12°$ both vertically and horizontally is excluded to avoid a beam halo. Schematic view of the spectrometer is shown in Fig. 7. It consists of 3 main parts as follows and the list of detectors is shown in Table 2.

GEM Tracker
To measure momenta of electrons and positrons, a GEM-based micro-pattern gas detector is used. The GEM tracker is originally developed for the COMPASS experiment [16] for high rate counting and was working up to 25 kHz/mm^2 while the highest counting rate in the E16 experiment is 5 kHz/mm^2. The GEM tracker is composed of three layers and each layer is respectively placed at the radius 200 mm, 400 mm, and 600 mm in a magnetic field. Each layer consists of a triple GEM stack and readout strips. The points which the incident particle passes through are detected. We can determine the passage of the incident particle by using these points and can calculate the momentum of the traversing particle. The E16 experiment requires the mass resolution of 5 MeV. It means that GEM tracker should achieve approximately 100 μm spacial resolution.

HBD
Getting pure electron samples, we need a detector which has high electron identification capability. In the E16 experiment, a Hadron Blind Detector (HBD), which was originally developed in the PHENIX experiment, is used as the electron ID counter. The main purpose of the HBD is electron

Detector	Radius (mm)
GEM Tracker 1st Layer	200
GEM Tracker 2nd Layer	400
GEM Tracker 3rd Layer	600
HBD	600-1100
Lead Glass Counter	1140-1700

Table 2: List of the detectors.

identification from hadrons. To avoid miss identification of hadrons which makes the background, a hadron rejection factor of 100 is required in the momentum region of electrons from light vector meson decays. The HBD is placed from the radius of 600 mm to the radius of 1100 mm. This master thesis focus on development. Performance of the HBD and fundamental information about the HBD can be found in the next chapter.

Lead Glass Counter

Lead Glass counter is used as EM calorimeter. The E16 experiment will achieve sufficient electron ID capability with combination of the HBD and the Lead Glass EM calorimeter. A hadron rejection factor of 25 is required.

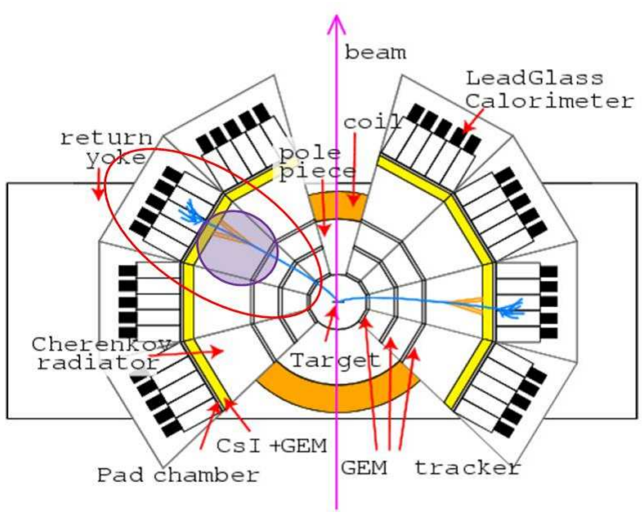

Fig. 7: Schematic view of the new spectrometer. The spectrometer consists of 26 segments and the red circle represents one segment. One segment consists of a GEM tracker, a HBD and a lead glass counter. The purple area is the HBD in one segment.

3 Development of the HBD

The HBD is a mirror-less and window-less Čerenkov detector operated with CF_4 and was originally developed by the PHENIX group [17]. The E16 experiment use the HBD to identify e^+e^- pairs generated by the light vector meson decays. It has a 50 cm length of a radiator directly coupled to a readout element consisting of a triple Gas Electron Multiplier (GEM) stack with CsI photocathode evaporated on the top surface of the top GEM and pad readout at the bottom of the stack. The detector concept is elegant and complicated, thus many elements should be developed. In this chapter each component is described separately. Before explaining the HBD, GEM is described at first since GEM is a main component of the HBD.

3.1 Gas Electron Multiplier

Gas Electron Multiplier (GEM) is a thin insulating foil which have electrodes on both sides and many of small holes, originally developed at CERN. Typical thickness of the foil and the electrodes is 50 μm and 4 μm, respectively. Typical hole size is 70 μm and the distance between holes is 140 μm. By applying suitable voltage between the electrodes, strong electric field is formed in the holes. An electron drawn into a hole is accelerated by the electric field and an electron avalanche happens in the hole if amplification gas is filled up. Fig. 8 shows the enlarged view of the GEM surface.

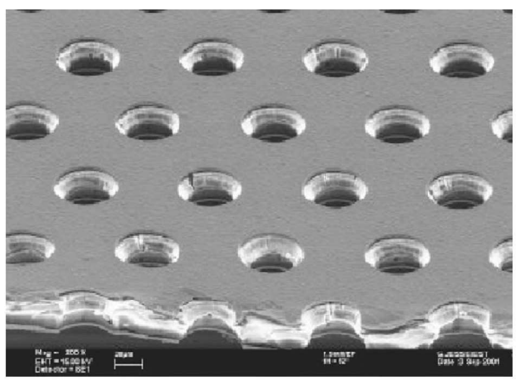

Fig. 8: Enlarged view of typical GEM.

3.2 Operation Principle of the HBD

A schematic drawing of the HBD is shown in Fig. 9. Electrons having the momentum exceeding a some threshold can emit Čerenkov radiation in CF_4. Refractive index of CF_4 is approximately $1 + 620 \times 10^{-6}$ [18], whereas heavier particles like pion don't emit Čerenkov radiation in the same momentum region of electron. The threshold momenta of electron and pion in CF_4 are described in Table 3. A Čerenkov photon is converted into a photoelectron by CsI which is evaporated on the top of the GEM stack. Then the photoelectron is amplified by the GEM stack and signals are collected by the pad readout. A mesh is placed over the top of the GEM stack and is used to form the electric field between the mesh and the top GEM. A gap between the mesh and the top

	mass (MeV)	threshold momentum (MeV)
e	0.5110	1.5×10^1
π	139.6	4.2×10^3

Table 3: The threshold momentum of Čerenkov radiation in CF_4

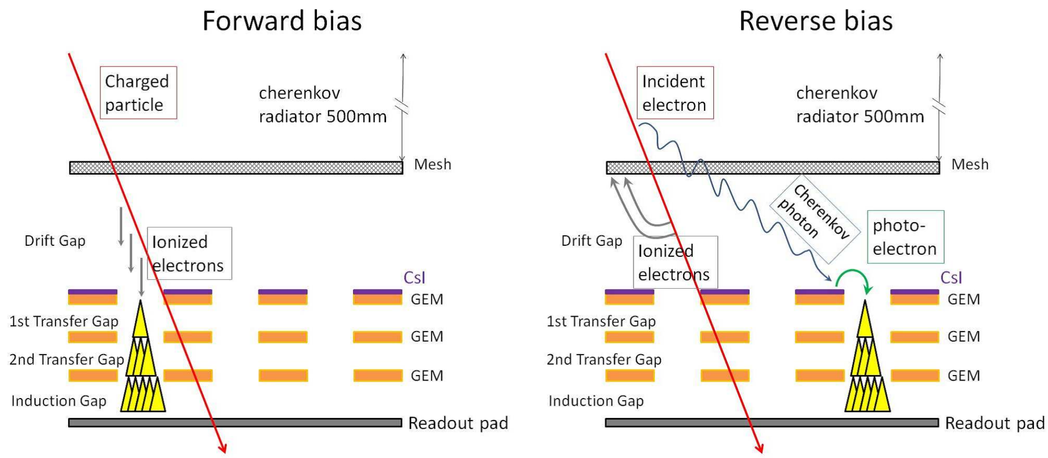

Fig. 9: Schematic drawing of HBD. Triple GEM stack operated in the standard forward bias mode (left) and in the hadron-blind reverse bias mode (right).

GEM is called drift gap and electric field in the drift gap is called the bias field. The bias field can manipulate the flow of ionization electrons generated in the drift gap by an incident particle. The hadron blindness property of the HBD is achieved by operating the detector in the so-called reverse bias mode as opposed to the standard forward bias mode (see Fig. 9). In the reverse bias (RB) mode, the mesh is set at a lower negative voltage with respect to the top GEM and consequently the ionization electrons generated by a charged particle in the drift gap are mostly repelled toward the mesh (see Fig. 9). Consequently, the possible signals produced by a charged particle which doesn't emit Čerenkov radiation are limited to the following two cases.

1. the collection of ionization electrons generated in the drift gap which aren't swept into the mesh. These ionization electrons are subject to a 3-stage amplification.

2. the collection of ionization electrons produced in the first transfer gap (between the top and the middle GEMs). These ionization electrons are subject to a 2-stage amplification.

The ionization electrons produced in the second transfer gap and in the induction gap (between the bottom GEM and the readout pads) generate a negligible signal since they experience one and zero stages of amplification, respectively.

3.3 Development of Components

To accomplish good separation of electron and hadron, we need to minimize the collection of ionization electrons produced in drift gap and in the first transfer gap and to increase the number of photoelectrons pulled into holes of the top GEM. The minimization of the collection of ionization electrons generated in the transfer gap is mainly achieved by high amplification of the top GEM, when the photoelectrons are sufficiently amplified by the top GEM, ionization electrons produced in the transfer gap which don't experience top GEM amplification are negligible compared with the amplified photoelectrons. Of course, this method doesn't decrease ionization electrons produced in the drift gap and these residual ionization electrons determine detector performance. Two methods can be considered to increase the number of photoelectrons pulled into holes of the top GEM, (1) making a CsI photocathode of high quantum efficiency. As quantum efficiency increases, the number of photoelectrons increases and effect of ionization electrons decreases. (2) increasing collection efficiency of photoelectrons. Photoelectrons produced on the surface of the CsI photocathode aren't always pulled into holes of the top GEM. There are possibilities that photoelectrons are pulled toward the mesh or are absorbed by the surface of the top GEM immediately after they are produced. The probability that the photoelectrons repelled into the mesh strongly depends on the bias field. The absorption probability of the photoelectrons depends on the gas property and strength of electric field at the surface of the photocathode, since this phenomenon is caused by a backscattering of photoelectrons by gas molecules near the surface of the photocathode. The electric field at the surface of the photocathode depends on the applied voltage across the top GEM, hole shape of the top GEM and thickness of the top GEM. Thus we need to measure the collection efficiency for various GEMs which differ hole shape and thickness.

These phenomena mentioned above are summarized as follows.

1. the collection of ionization electrons produced in the drift gap
   $\rightarrow$ is inevitable and determine the final detector performance.

2. the collection of ionization electrons produced in the first transfer gap
   $\rightarrow$ relatively decrease with high amplification of the top GEM.

3. the number of photoelectrons
   $\rightarrow$ increases by making a CsI photocathode of high quantum efficiency.

4. the collection efficiency of photoelectrons
   $\rightarrow$ increases by setting an optimum bias field and an optimum electric field at the surface of the photocathode.

These components are measured and developed in the laboratory and are described in following chapters.

4 Quantum Efficiency of CsI

A larger number of collected photoelectrons is directly related to a better electron identification efficiency and hadron rejection factor. If the larger number of photoelectrons can be achieved, we can keep a high electron detection efficiency and high hadron rejection factor. Therefore, as mentioned previous chapter, R&D of photocathodes having high Quantum Efficiency (QE) is one of our concerns. A thin layer of CsI is evaporated on GEM electrode surface and GEM becomes a photosensitive. We handled CsI-coated GEMs with extreme care, since CsI is a deliquescent substance and GEM itself very sensitive to dust. This chapter describes preparation of CsI photocathodes and measurements of absolute QE of CsI photocathodes.

4.1 CsI Photocathode Preparation and Handling

GEM foils are made photosensitive by the vacuum evaporation of a thin layer of CsI on the GEM electrode surface. This CsI layer is not chemically stable on the GEM electrode surface which is made of Cu, since iodine is more tightly bound with Cu than Cs. For this reason, we produced a special subset of the GEMs whose metallic surface was overlayed with Ni (1 μm) and then Au (0.05 μm) by electroplating. Ni was plated as a diffusion barrier since Ni has a larger ionization tendency than Cu. These GEMs (we call Au GEM) show the same gain and stability as the standard Cu GEMs. Fig. 10 and 11 show the photograph of a standard Au GEM and a Cu GEM. For study of the absolute QE, we used only 100 $\times$ 100 mm^2 GEMs.

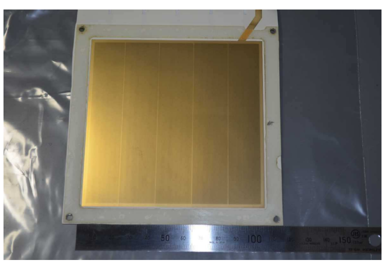

Fig. 10: Photograph of a Au GEM.

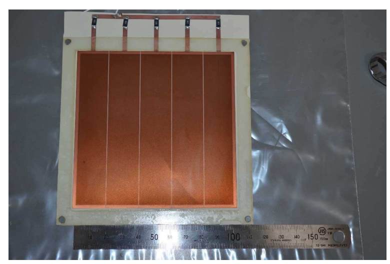

Fig. 11: Photograph of a Cu GEM.

Generally, powder and crystal forms of CsI are used for evaporation. The crystal CsI shows higher absolute QE than the powder CsI [19] since the powder CsI may have high surface contamination because surface area of the CsI powder is larger than that of the CsI crystal. Therefore, we used only the crystal form of CsI. We prepared two different kinds of CsI crystals. One is a commercially available one (Furuchi kagaku) and the other is a chunk which is scraped from a pure CsI calorimeter as shown in Fig. 12.

Fig. 12: CsI crystals: a commercially available (left), a scraped one (right). We quarry a chunk of CsI crystal by ourselves from the CsI calorimeter by a cutter.

A evaporator we used is covered by a glass bell jar and equipped with a thermal evaporation source, a quartz thickness monitor, a GEM holder and a shutter. Fig. 14 is a photograph of our evaporator.

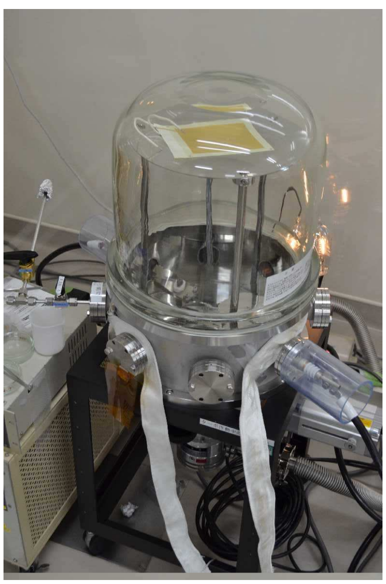

Fig. 13: Photograph of the evaporator.

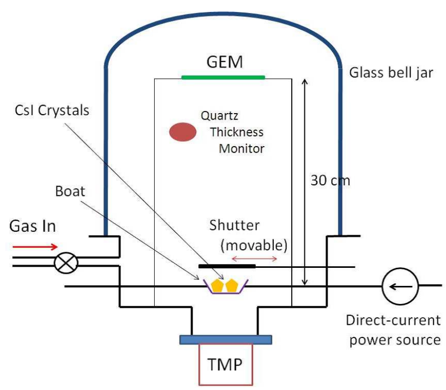

Fig. 14: Sketch of the evaporator.

CsI crystals are placed on the thermal evaporation source called "boat" which is made of Mo with high melting point. The boat is heated by passing an electric current through it and then the CsI is evaporated and deposited in one side of the Au GEM surface. The quartz thickness monitor positioned near the GEM surface is used to determine the deposition rate of the CsI. The GEM holder is placed 30 cm above the boat to avoid the non-uniformity of the CsI thickness on the GEM surface. A movable partition plate located between the boat and the GEM holder can control flow of CsI molecules and ensure the thickness of the CsI layer on the GEM surface. Whole system can be pumped by a turbo molecular pump and all procedures are performed with care in a clean room. The standard preparation procedure consist of following steps:

1. All GEMs are carefully cleaned with pure nitrogen gas spray, which have static electricity elimination function, in order to blow polar as well as non-polar dusts off the GEM surfaces.

2. A GEM and CsI crystals are mounted into the evaporator. The total amount of the CsI crystals is 0.6 g, which ensures enough thickness in spite of possible non-uniformities of the coating. In this process we have to take off the glass bell jar and thus the CsI crystals are exposed to air for at least 3 min.

3. Prior to deposition, whole system is pumped and heated by a heater belt for degassing at temperature of 310-320 K for a minimum duration of 12 h. Before deposition the heating is switched off.

4. Then evaporation process is performed at a vacuum pressure $< 4 \times 10^{-6}$ Torr. The rise rate of the current through the boat is approximately 2 A/min and the CsI crystals start to evaporate at the boat current of approximately 40 A. In the first 30 seconds of the evaporation the shutter is closed for blowing the CsI crystal surfaces which are exposed to water vapor.

5. Then the shutter is open and the deposition starts. The deposition rate of the CsI is kept near 1.5 nm/s. The final thickness of the CsI layer is typically $\sim$350 nm. Reflective photocathodes exhibit a quantum efficiency saturates as a function of the cathode thickness. For CsI, this saturation point is found at $\sim$200 nm thickness [17].

6. After the end of the evaporation process the GEM remains in a vacuum at a vacuum pressure $< 4 \times 10^{-6}$ Torr for at least 12 h.

7. The whole system is vented with dry nitrogen ($H_2O < 3$ ppm). The glass bell jar is removed and then the CsI-coated GEM is quickly transferred to a pass box which is coupled to a glove box. Fig. 15 shows the pass box and the glove box. The pass box is pumped down to approximately 3 Pa immediately after the CsI-coated GEM is put into the pass box. In this process the CsI-coated GEM is exposed to air for approximately 10 seconds.

Fig. 15: Large glove box.

8. The pass box is vented with dry nitrogen which circulated in the glove box (H_2O < 20 ppm) and then the CsI-coated GEM is transferred to the glove box.
9. Inside the glove box the CsI-coated GEM is mounted in a G10 plate as shown in Fig. 16 to protect the photocathode from physical damages. The CsI-coated GEM with the G10 plate and a desiccant are put into a bag together.

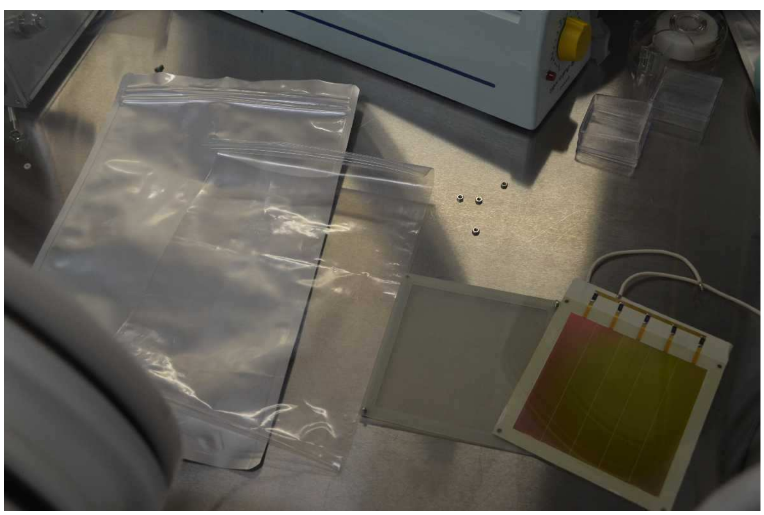

Fig. 16: CsI-coated GEM with a G10 plate. The CsI-coated GEM is mounted in the G10 plate at first and then packed into the bag with a desiccant.

10. The bag is transferred to a desiccator and preserved in it until measurement of the absolute QE start. This preservation method ensures that the absolute QE of CsI coated GEM shows no degradation for at least a few months.

11. For absolute QE measurement, the CsI-coated GEM is mounted into a chamber with another glove box as shown in Fig. 17, which is smaller than the previously mentioned one. This process is performed in dry nitrogen.

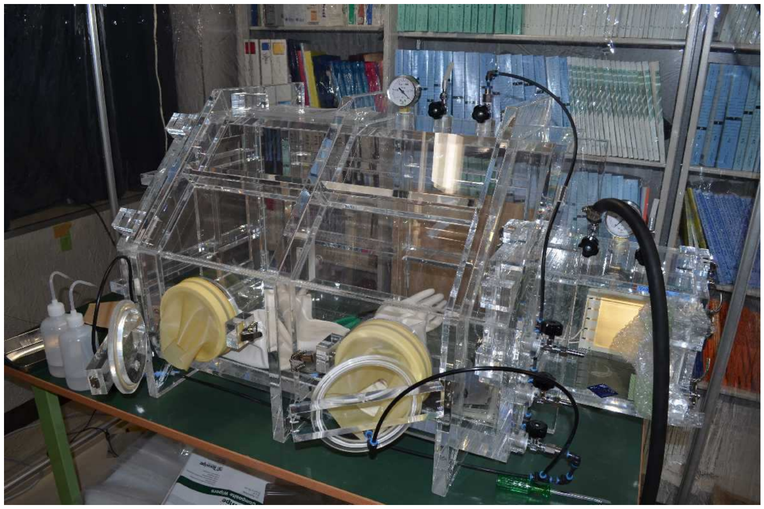

Fig. 17: Small glove box.

12. The chamber is sealed in the glove box and then flanged to an absolute QE measurement system. The chamber is sealed with no gas flow during the process in which the chamber is transferred to the absolute QE measurement system from the glove box. This process takes approximately 3 min.

The procedure outlined above ensures that the CsI-coated GEMs are exposed to air for only 10 seconds between the production and the first absolute QE measurement and this exposure shows no degradation of the photocathode [20]. It was applied to all samples shown in subsequent sections.

4.2 Measurement system of the absolute QE

Measurement of the absolute QE is very important since the absolute QE of CsI photocathode is directly reflected on performance of the HBD. The absolute QE of CsI photocathode was measured by a large number of groups. Most of the measurements are in good agreement. However, only a few groups measured at wavelengths below 140 nm (or photon energy above 8.3 eV). Since CF_4 is transparent up to 11 eV, it is very important to extend measurement of the absolute QE of CsI photocathode as much as possible. The determination of the absolute QE requires an absolutely calibrated light source which also have enough light intensity in wide range. Unfortunately, it is not available in most laboratories. Therefore, usually a relative method is used, the measurement of the relative response of the sample (CsI photocathode) to a well-known reference. In our measurement, we used a calibrated photomultiplier tube as a reference. The experimental setup we used for the measurement is shown in Fig. 18 and Fig. 19. It consists of an optical system box and a detector chamber.

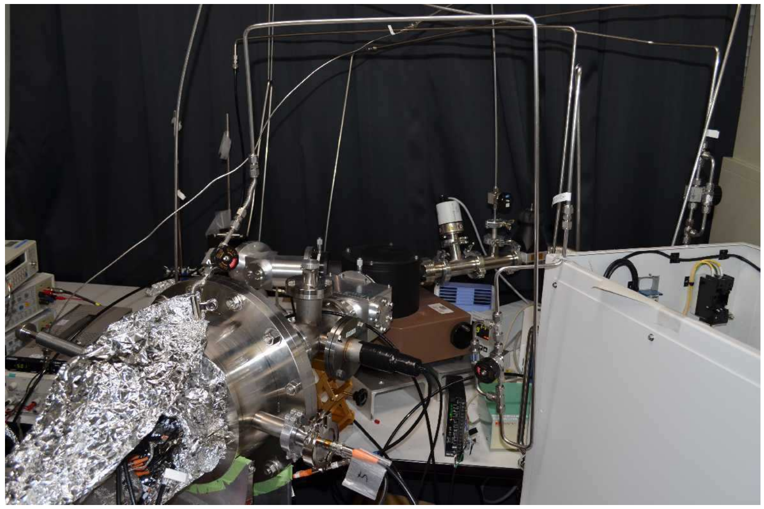

Fig. 18: The set up for QE measurement.

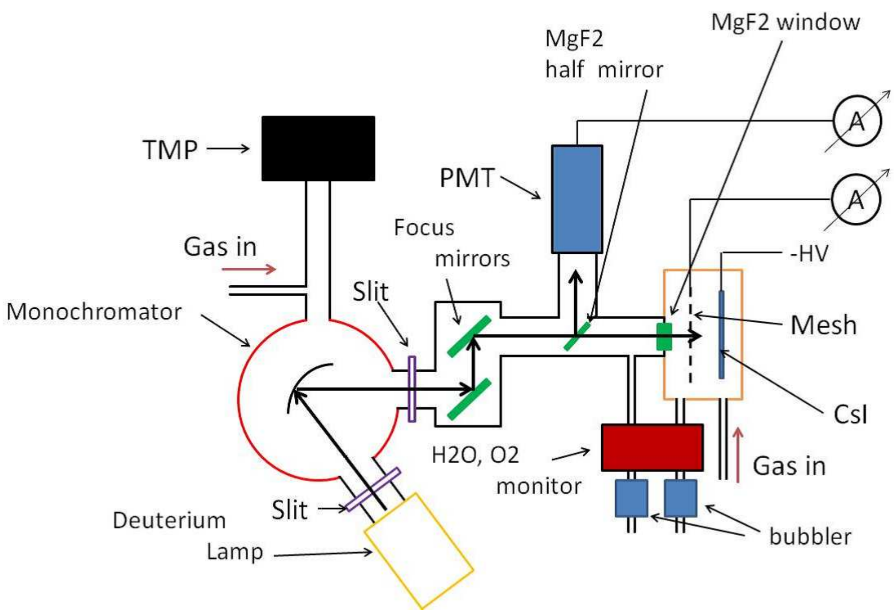

Fig. 19: Sketch of QE measurement. The whole system can be factorized into two components: an optical system box and a detector chamber. These are separated by a MgF_2 window.

An optical system box includes a vacuum ultraviolet (VUV) monochromator (Shinku-kogaku VMK-200-I) equipped with a deuterium lamp (Hamamatsu L10388, 115-400 nm shown in Appendix), coupled via a MgF_2 window (cut-off at 110 nm) to a detector chamber. The optical system box also includes optical slits, focusing mirrors, a MgF_2 half mirror. The optical slits are provided on the monochromator to control the flux. The focusing mirrors collimate the light and the half mirror splits the beam between photomultiplier PMT1 (Hamamatsu R6836) and the detector chamber. PMT1 is a absolutely calibrated CsTe photocathode photomultiplier tube and serves as a reference and the quantum efficiency were provided by a manufacturer. The quantum efficiency of all PMTs which we used is shown in Appendix. To have enough current of the PMT1, we used CsTe photocathode photomultiplier tube which has the larger absolute quantum efficiency around 200 nm than that of a CsI photocathode photomultiplier tube. The detector chamber contains a GEM foil (100×100 mm^2) on which a 350 nm layer of CsI are evaporated. Above the GEM foil and at a distance 4 mm from it is a mesh electrode which is at a positive voltage with respect to the GEM foil to pull photoelectrons from the CsI photocathode toward the mesh. The size of the light spot on the photocathode of PMT1 and the GEM foil are both 3 mm across in diameter, which is sufficiently small for photoelectric surfaces.

Impurities such as water vapor and oxygen in the measurement system can reduce the photon flux. Both water vapor and oxygen have strong absorption peaks in a spectral range of sensitivity of the CsI photocathode Fig. 20.

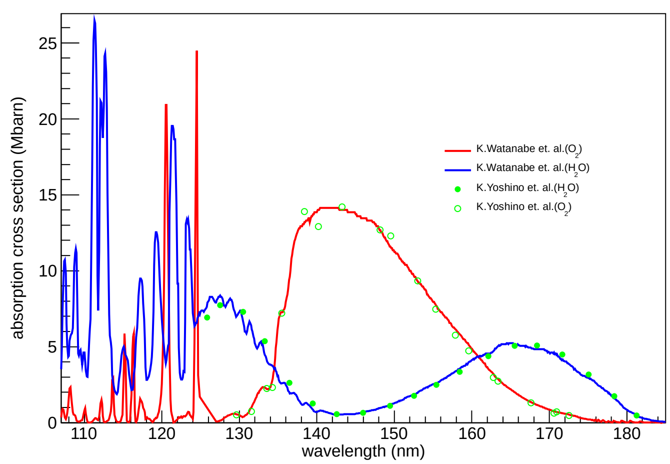

Fig. 20: Photon absorption cross section for water vapor and oxygen over the wavelength range of sensitivity of CsI to Čerenkov light. Solid curves measurements are from [21]. Other measurements are from [22, 23].

The main source of oxygen contamination is a leak. The main source of water is from outgassing within the system. Water contamination can be decreased by keeping the optical system box in a high vacuum in a few days. Applying VUV light in a vacuum, it's expected that a significant loss in light intensity due to the buildup of deposits on the beam optics, so we operated the beam optics at atmospheric pressure under a flow of pure argon which is transparent gas in VUV wavelength range. The cut-off energy of argon is ∼9 eV. For the above two reasons the optical system box can be pumped by a turbo molecular pump and also can be purged with pure argon.

Our detector chamber was not able to be pumped due to its small leak. However this leak has no influence on the water and oxygen level when gas flows in the detector chamber. Therefore, prior to the measurement, the detector chamber volume was carefully replaced with pure CF_4 at

	detector	optical system
Water vapor	5 ppm	1.5 ppm
Oxygen	2 ppm	1 ppm

Table 4: Impurity levels in QE measurement.

atmospheric pressure at least 10 times. Both water and oxygen contamination in the whole system are monitored and we performed this measurement at less than those values which are shown in Table 4. Those values ensure the loss of the light intensity is less than 1 % over the every wavelength of our measurement (120-200 nm).

4.3 Derivation of the absolute QE

We measured the photocurrent of PMT1 and the CsI by ammeters (ADCMT 8340A). To measure the photocurrent of PMT1, we operated PMT1 in photodiode mode (gain = 1). The photocurrent of the CsI is measured in following two different ways. One called "GEMh mode" is that the GEM foil is ground voltage and the terminal of the ammeter is connected to the GEM foil while the mesh is positive voltage. The other called "Mesh mode" is that the mesh is ground voltage and the terminal of the ammeter is connected to the mesh while the GEM foil is negative voltage. Applied voltage across the GEM is set to zero in both modes to ensure that photoelectrons may not be pulled into GEM holes. These two modes give the same QE, as shown in a following section, which suggests that there is no photoelectron loss when the photoelectrons drift in CF_4 from the CsI photocathode toward the mesh. The measurements were done over the wavelength range of 120-200 nm (E = 6.2-10.3 eV). The measured photocurrent of the CsI and photomultiplier PMT1 is shown in Fig. 21.

The absolute QE of the CsI photocathode at a given wavelength λ is given by

$$\mathrm{QE}_{\mathrm{CsI}}(\lambda) = \left(\frac{I_{\mathrm{CsI}}(\lambda)}{I_{\mathrm{PMT1}}(\lambda)}\right) * \left(\frac{R}{T}(\lambda)\right) * \left(\frac{1}{\epsilon_{\mathrm{m}} * \epsilon_{\mathrm{G}}}\right) * \mathrm{QE}_{\mathrm{PMT1}}(\lambda) \tag{3}$$

where $I_{\mathrm{CsI}}(\lambda)$ is the CsI photocathode current measured at wavelength λ, $I_{\mathrm{PMT1}}(\lambda)$ is the PMT1 photocurrent at λ, $\frac{R}{T}(\lambda)$ is a ratio of the beam intensity on the PMT1 photocathode to the beam intensity on the GEM foil, which we have to measure in advance, ϵ_{m} is the mesh transparency ($\epsilon_{\mathrm{m}} = 0.883$), ϵ_{G} is the opacity of the CsI photocathode due to the GEM hole which depends on configuration of the GEM hole, $\mathrm{QE}_{\mathrm{PMT1}}(\lambda)$ is the absolute QE of PMT1 at λ.

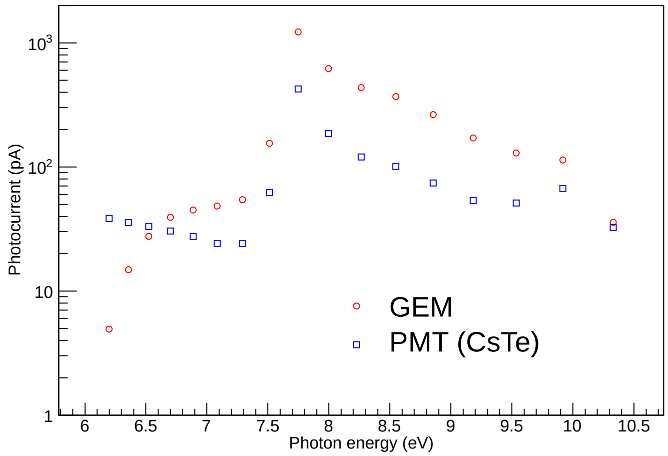

Fig. 21: Photocurrent from a CsI photocathode and a reference photomultiplier as a function of wavelength. These values depend on the intensity of the deuterium lamp as well as the QE of each detector (PMT and our CsI photocathode).

4.4 Measurement of R/T

We measure $\frac{R}{T}(\lambda)$ by setting a absolutely calibrated photomultiplier tube PMT2 (Hamamatsu R6836) on MgF_2 window instead of the detector chamber. $\frac{R}{T}(\lambda)$ is given by

$$\frac{R}{T}(\lambda) = \frac{I_{\mathrm{PMT2}}(\lambda)}{I_{\mathrm{PMT1}}(\lambda)} * \frac{\mathrm{QE}_{\mathrm{PMT1}}(\lambda)}{\mathrm{QE}_{\mathrm{PMT2}}(\lambda)} \tag{4}$$

where $\mathrm{QE}_{\mathrm{PMT1}}(\lambda)$ and $\mathrm{QE}_{\mathrm{PMT2}}(\lambda)$ are the absolute QE of the PMTs at λ respectively, $I_{\mathrm{PMT2}}(\lambda)$ and $I_{\mathrm{PMT1}}(\lambda)$ are the photocurrent of the PMTs at λ respectively. $\frac{R}{T}(\lambda)$ include both the MgF_2 half mirror and the MgF_2 window. To evaluate the systematic error in $\frac{R}{T}(\lambda)$, we swap the PMTs and use the CsI photocathode photomultiplier tube PMT3 (Hamamatsu R6835). If PMT1 is flanged into the side of the optical system and PMT2 is flanged into the front of the optical system, we call this setup (PMT1-S PMT2-F). Fig. 22 shows the value of $\frac{R}{T}(\lambda)$ plotted as a function of the photon energy. The value of $\frac{R}{T}(\lambda)$ is determined by fitting a Gaussian to the current ratio. We write the mean of the Gaussian as Mean and the sigma of the Gaussian as σ. Even if the ratio of the current is stable, the current itself can change with time due to time dependence of the light intensity as shown in Fig. 23.

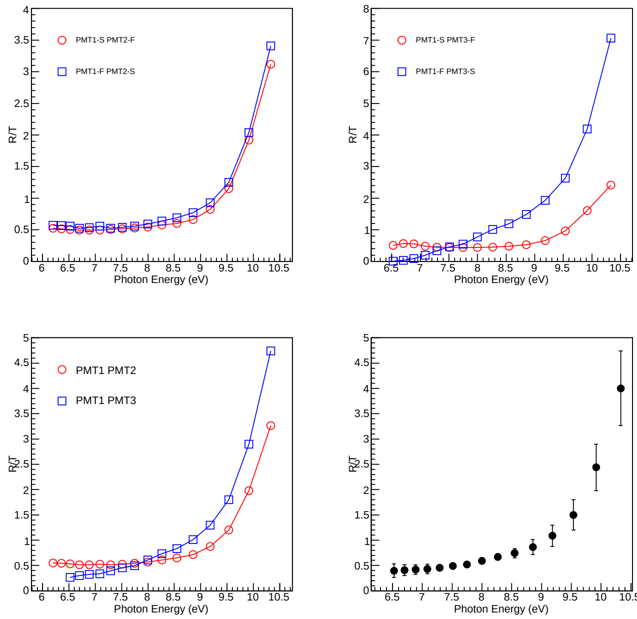

Fig. 22: R/T: the ratio of the light intensity on the side of the box to the front of the box, which includes both MgF_2 half mirror and MgF_2 window. Upper left panel: red circles means PMT1 is flanged into the side of the box and PMT2 is flanged into the front of the box instead of the detector chamber and blue squares are swapped one. Upper right panel: red circles means PMT1 is flanged into the side of the box and PMT3 is flanged into the front of the box instead of the detector chamber and the blue squares are swapped one. Lower left panel: The averages of each configuration. Lower right panel: final result of R/T.

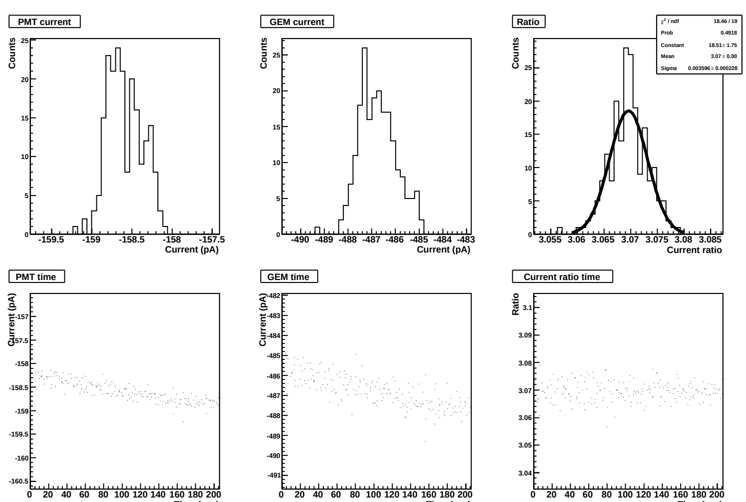

Fig. 23: The upper left and middle panels: histogram of photocurrent from reference PMTs. The upper right panel: histogram of the photocurrent ratio. The lower left and middle panels: plots of time dependence of photocurrent. The lower right panel: plot of time dependence of photocurrent ratio.

Therefore, we are not able to use the simple form of propagation of errors for an estimation of the statistic error of $\frac{R}{T}(\lambda)$ since the current of PMTs correlate with each other via the light intensity. Thus, the estimation of the relative statistic error was taken to be σ/Mean and this overestimates the statistic error. However, this overestimated statistic errors small enough than the systematic errors caused by the swap and exchange of the PMTs. We performed this measurement four times with different setups: (PMT1-S PMT2F), (PMT1-F PMT2-S), (PMT1-S PMT3-F) and (PMT1-F PMT3-S). The values of $\frac{R}{T}(\lambda)$ in (PMT1-S PMT2-F) and (PMT1-F PMT2-S) are shown in the left of the upper panel of Fig. 22 and those of in (PMT1-S PMT3-F) and (PMT1-F PMT3-S) are shown in the right of the upper panel of Fig. 22. (PMT1-S PMT2-F) and (PMT1-F PMT2-F) are good agreement with each other, however (PMT1-S PMT3-F) and (PM1-F PMT3-S) shows very different result. This may be caused by the fact that PMT1 and PMT2 are the same model PMTs and may show the same inclination about the deviation of the absolute QE from the values provided by a manufacture. The average of (PMT1-S PMT3-F) and (PMT1-F PMT3-S) and the average of (PMT1-S PMT3-F) and (PMT1-F PMT3-S) illustrated in the left of the lower panel show the difference between two configurations. This difference was taken to be a measure of the systematic error. A simple, non-weighted average was therefore taken as the best estimation of $\frac{R}{T}(\lambda)$, and an estimate of the total error was taken to be half of the difference between the two values. The final plot of $\frac{R}{T}(\lambda)$ is shown in the right of the lower panel of Fig. 22

4.5 Result of the absolute QE

Four results about absolute QE are shown in this section.

- We use two kinds of CsI crystals and investigate the difference about QE between these. To compare these with each other, we plot QE of each sample at wavelength of 160nm, in which the intensity of the deuterium lamp is most intense. Fig. 24 shows the result.

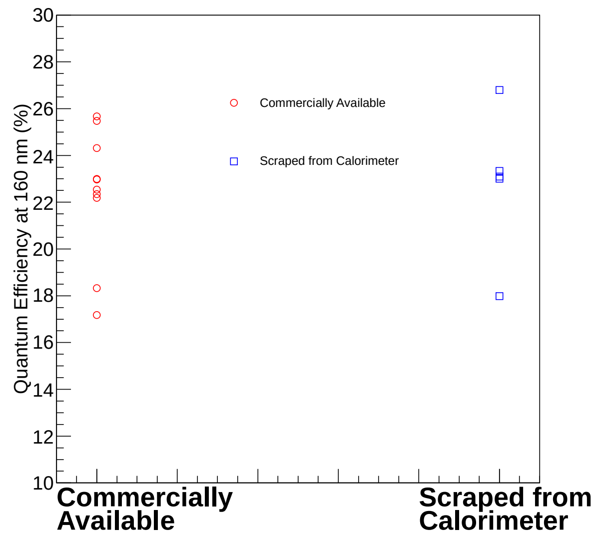

Fig. 24: The absolute QE at wavelength of 160 nm. Two different kinds of CsI crystals are used.

The average QE at 160 nm of the commercially available CsI crystal is 22.4 % and that of the scraped from pure CsI calorimeter is 22.8 %. We conclude that there is no difference between the two crystals and all CsI photocathodes mentioned in following sections are produced with evaporation of the CsI crystals scraped from the CsI calorimeter.

- As mentioned previously, CsI is a deliquescent substance, therefore preservation and handling process is a fatal issue in practice. An aging property of our CsI photocathode can be a criterion to determine how long our CsI photocathode is normally available in our measurement and whether or not our handling process is correct. We measure the absolute QE of the same photocathode two times and the result is shown in Fig. 25.

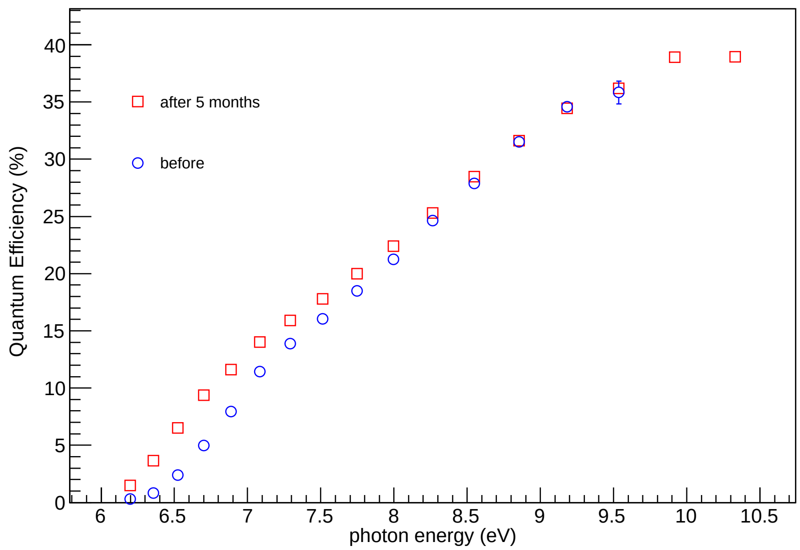

Fig. 25: Aging of the CsI photocathode. No degradation is observed.

The blue circles are measured in Dec. 2011 and the red squares are measured in July 2011. In low energy region there are differences of absolute QE between two points, namely the red points shows systematically high QE. So far, we can not find a reason of this phenomenon that aged CsI photocathodes tend to show a little higher QE. Anyway no degradation is observed in CsI photocathode, which indicates our preservation and handling process ensures that the absolute QE doesn't change in at least a few months. E16 experiment will take 100 shifts (33 days) as the first beam time and thus we expect the CsI photocathodes in the spectrometer will stably work without degradation of the absolute QE.

- Fig. 26 shows the absolute QE measured in GEMh mode and in Mesh mode. There is no difference between two methods, which means that once successfully extracted photoelectrons are always transported into the mesh along the electric field without any loss in the gas. Based on this result, all values of the absolute QE, which are referred in following chapters, are measured in Mesh mode where the terminal of the ammeter is connected to the mesh.

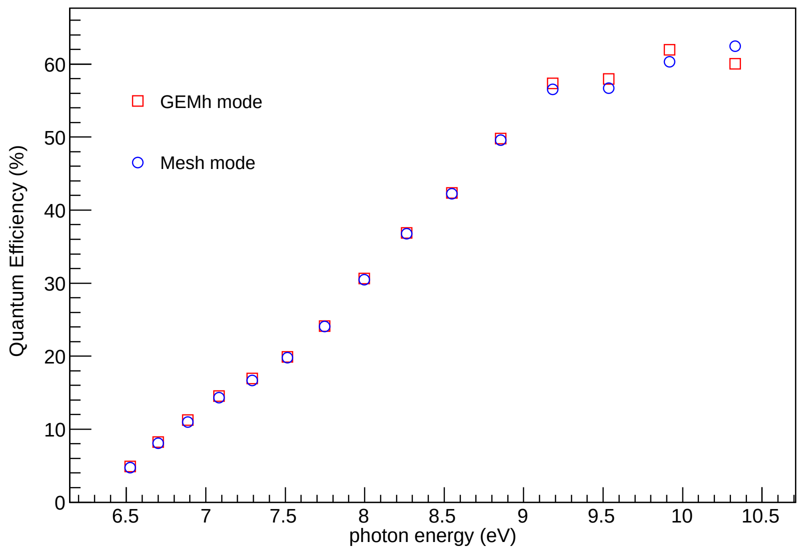

Fig. 26: The absolute QE measured in GEMh mode and Mesh mode.

- Fig. 27 shows a representative sample of current results. The blue squares represent measurement of [24], the red squares represent measurement of Weizmann which is the best result until the present and the black dots represent our measurement. Our measurement and Weizmann measurement are in reasonable agreement with each other over the wavelength range of 120-200 nm (E = 6.2-10.3 eV), while the blue squares shows high QE in low energy region. However, these difference does not cause a difference on the final number of photoelectrons since the number of Čerenkov photons is mainly determined in high photon energy region. The number of Čerenkov photons emitted by a charged particle of charge ze is given by

$$\frac{dN}{dxd\lambda} = \frac{2\pi\alpha z^2}{\lambda^2}(1 - \frac{1}{\beta^2 n^2(\lambda)}) \tag{5}$$

where N is the total photon yield, λ is wavelength, α is the structure constant and n is the refractive index of the medium that is a function of the photon energy, or equivalently to λ. For particular case of an electron moving along a track of length L within a spectral region defined by wavelength λ_1 and λ_2 we will have

$$N = \int_0^L \int_{\lambda_1}^{\lambda_2} \frac{dN}{dxd\lambda} dxd\lambda \tag{6}$$

$$= 2\pi\alpha L(\frac{1}{\lambda_2} - \frac{1}{\lambda_1})(1 - \frac{1}{\beta^2 n^2}) \tag{7}$$

where n is treated as a constant for simplicity. Thus the low energy region, which is equal to long-wavelength region, contributes little to the total photon yield.

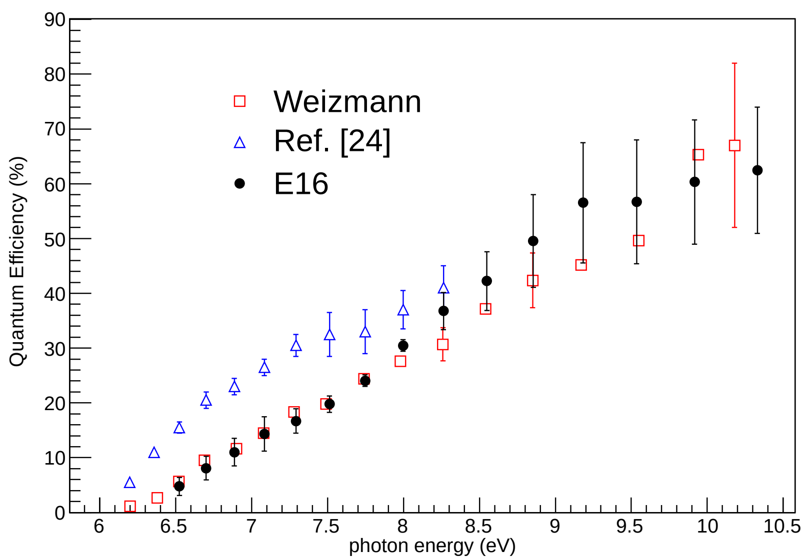

Fig. 27: Absolute QE as a function of photon energy.

5 Photoelectron Collection Efficiency

Photoelectron collection efficiency of a CsI photocathode is also important as QE of a CsI photocathode since it is directly related to the number of photoelectrons we can observe. Photoelectrons which is extracted from a CsI photocathode are not always transported into GEM holes. This transportation process is very important for the performance of the HBD and we perform systematic measurement about this process. The purpose of this study is to investigate the various parameters affecting the photoelectron collection efficiency in order to optimize the performance of the HBD.

5.1 Overview

First of all, we define the photoelectron collection efficiency (CE) as the ratio of the number of photoelectrons which are collected and subsequently amplified in the gain region of the GEM detector to the number of photoelectrons which are produced at the photocathode for a given QE.
The collection efficiency can be factorized into two components: an extraction efficiency (EE) and a transport efficiency (TE).
The EE gives the fraction of photoelectron that are extracted from the CsI photocathode without backscattering processes within the gas. Photoelectrons produced in the photocathode must elastically collide with gas molecules and a scattered photoelectron is most likely to be forward scattered but there is a small chance that it will be backscattered. Backscattered photoelectrons go toward the surface of the photocathode and finally absorbed by the surface of the photocathode. Therefore, the successfully extracted photoelectrons drift along the electric field of the CsI photocathode surface.
The TE is the probability that a extracted photoelectron is successfully transported through the gas to the gain region. Thus, a successfully transported photoelectron is always amplified by the 1st layer of GEM detector. The overall collection efficiency can be expressed as the product of the two terms $\epsilon_{\mathrm{CE}} = \epsilon_{\mathrm{EE}} * \epsilon_{\mathrm{TE}}$. Fig. 28 illustrates the role of each efficiency. The EE has been studied by a number of authors, which suggest the EE mainly depends on the gas property. Thus, we can not expect improvement of the EE since it is mainly determined by the gas and understanding the TE is a main concern in this section.

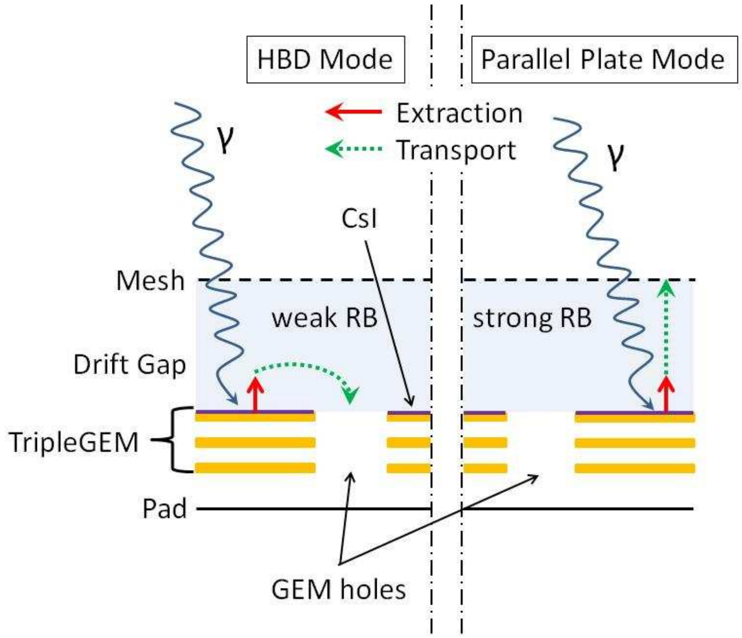

Fig. 28: Operation of a CsI photocathode GEM detector in HBD mode and in parallel plate mode. Red arrows indicate photoelectron extraction and blue arrows indicate photoelectron transport. The drift gap field (E_{D}) is set to slight reverse bias (RB) in normal HBD operation and strong RB in parallel plate operation.

5.2 Measurement method of the Transport Efficiency

The HBD which uses CsI photocathode GEM detectors leave signals when the CsI photocathode detect photons and the number of electrons of N we finally observe is given by

$$N = \int L(\lambda) * \mathrm{QE_{vac}}(\lambda) * \epsilon_{\mathrm{EE}}(\lambda) d\lambda * \epsilon_{\mathrm{TE}} * G \tag{8}$$

where $L(\lambda)$ is the light intensity at wavelength λ, $\mathrm{QE}_{vac}(\lambda)$ is a absolute QE of a CsI photocathode measured in a vacuum, which is free from backscattering process, and G is a effective gain of the GEM detector which we can measure by using ^{55}Fe spectrum. Therefore, If we know the exact light intensity, we can deduce $\epsilon_{\mathrm{EE}} * \epsilon_{\mathrm{TE}}$. Furthermore, we can deduce the TE since in our measurement the absolute QE of a CsI photocathode was already measured in CF_4 in parallel plate mode that the photoelectrons are extracted from the CsI photocathode and transported into the mesh without any amplification as shown if Fig. 28. In CF_4 parallel plate mode where we performed the absolute QE measurement, the photoelectrons must suffer from the backscattering process within CF_4, namely our absolute QE measurements in CF_4 inevitably include the backscattering effect and thus we can express $\mathrm{QE_{CF_4}}(\lambda) = \mathrm{QE_{vac}}(\lambda) * \epsilon_{\mathrm{EE}}(\lambda)$ where $\mathrm{QE_{CF_4}}$ is the absolute QE measured in CF_4.
We made two assumptions that the TE didn't depend on wavelength and the EE in HBD mode is the same as in parallel plate mode. Certainly, wavelength dependence of the TE is not so sure, however the assumption about the EE is quite natural, since the EE depends on the strength of the electric field of CsI photocathode. In HBD mode, the electric field of the top GEM surface is

mainly determined by the applied voltage across the top GEM and the electric field is approximately 3 kV/cm at the surface, whereas in parallel plate mode where the applied voltage across the top GEM is zero as mentioned previous section the electric field at the surface is only determined by the applied voltage in the drift gap. In parallel plate mode, the electric field at the surface should be the same as the average electric field in the drift gap since the applied voltage across the top GEM is zero, and the bias field is set to approximately 3 kV/cm. Fig. 29 and Fig. 30 show the electric field of CsI photocathode surface in normal HBD mode. Thus, if we use the absolutely calibrated light source, we can measure the TE.

A calibrated light source which exploits the scintillation emission band of CF_4 centered at ~ 160 nm ($\sigma \sim 5$ nm) [25] was designed and constructed to provide a known flux of photons to illuminate the CsI photocathode. This calibrated light source called "Scintillation Cube" is developed in PHENIX group [26]. A sketch of the scintillation cube is shown in Fig. 31. Inside the scintillation cube, ^{241}Am alpha particles traverse ~ 9.38 mm of CF_4 and produce scintillation light, thus providing a constant flux of 160 nm photons and illuminating the CsI photocathode.

A Solid State Detector (SSD: Ortec Model CU-011-025-300) provides a signal to trigger on the alpha particle. In addition, amplitude of the SSD signal provides the information about the energy deposition of the triggered alpha particle in CF_4. Prior to the measurement in CF_4, the SSD signal amplitude were calibrated in terms of energy by determining the signal amplitude in a vacuum, which corresponds to the initial energy of the alpha particle (~ 5.48 MeV). Thus, the total deposited energy in CF_4 is given by initial energy of the alpha particle minus the deposited energy in the SSD. The scintillation cube also includes an ^{55}Fe X-ray (5.89 keV) source to determine the gas gain of the GEM detector.

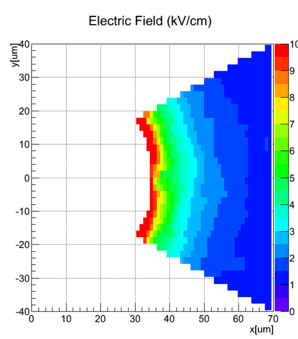

Fig. 29: Visualization of electric field of the 100 μm thickness GEM in the vicinity of a GEM hole which is 70 μm in diameter and hole pitch is 140 μm.

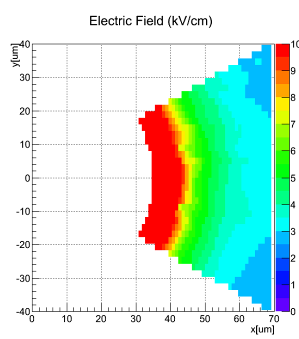

Fig. 30: Visualization of electric field of the 50 μm thickness GEM in the vicinity of a GEM hole which is 70 μm in diameter and hole pitch is 140 μm.

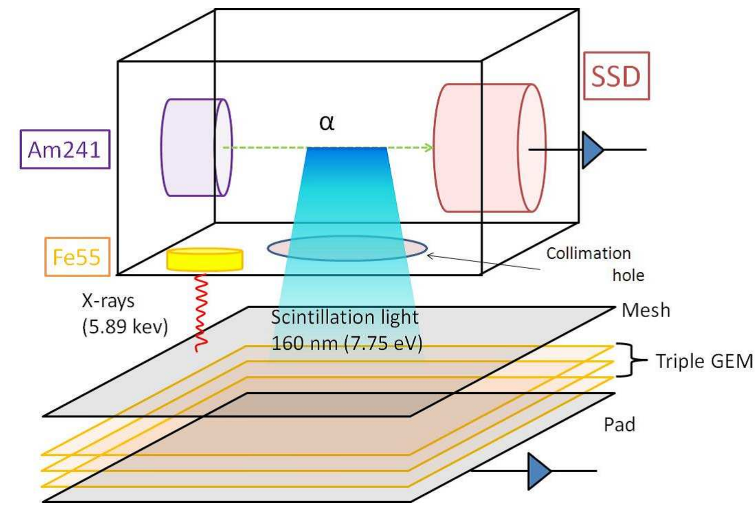

Fig. 31: Calibrated light source called "Scintillation Cube", illuminating a CsI photocathode of the GEM detector.

5.3 Photon Flux of Scintillation cube

Photon flux of the scintillation cube is measured using a absolutely calibrated CsI photocathode photomultiplier tube PMT3 (Hamamatsu R6835). The experimental setup is shown in Fig. 32. We measured the flux of scintillation cube around 160 nm with two methods.

5.3.1 Energy Deposition of the Alpha Particle in CF_4

A first method uses the energy deposition of alpha particle in CF_4. Fig. 33 shows the SSD signal amplitude in a vacuum and in CF_4. Both spectra are distorted in low energy since the SSD sometimes fails to collect all ionized electrons. The ^{241}Am alpha source has two alpha decay modes (5.485 MeV (85.2 %) and 5.443 MeV (12.8 %)) and is covered by very thin Au layer (100μg/cm^2) to seal it, which corresponds to the energy loss of 22.36 keV in both decay channels. The initial energy of the alpha particle is therefore 5463 keV and 5421 keV. The energy resolution of the SSD is 11 keV which are provided by a manufacture, therefore we can expect there are two peaks in ADC spectrum of alpha particle, however there is one peak in Fig. 33 due to bad energy resolution. The noise from an electronic circuit determined the resolution of this measurement. The weighted mean is taken to be the initial energy of the alpha particle, giving 5457 keV. To calibrate the ADC spectrum of the SSD in a vacuum, we fitted the ADC spectrum with a Gaussian and the mean of the Gaussian should correspond to the initial energy (5457 keV). We estimate the energy resolution of the measurement to the sigma of the Gaussian (39 keV). In CF_4, the energy deposition in the SSD shows rather broad and distorted distribution than in a vacuum due to the fluctuation of the interaction between the alpha particles and gas molecules. The ADC spectrum in CF_4 wasn't able to be fitted with a simple Gaussian and we estimate the average of the energy deposition as mean of the histogram. Thus, the mean energy loss in CF_4 is given by $5457 - 2019 = 3438$ keV. The photon yield in CF_4 in full solid angle N_{tot} is 314 ± 15 photons per MeV at atmospheric pressure [27]. The

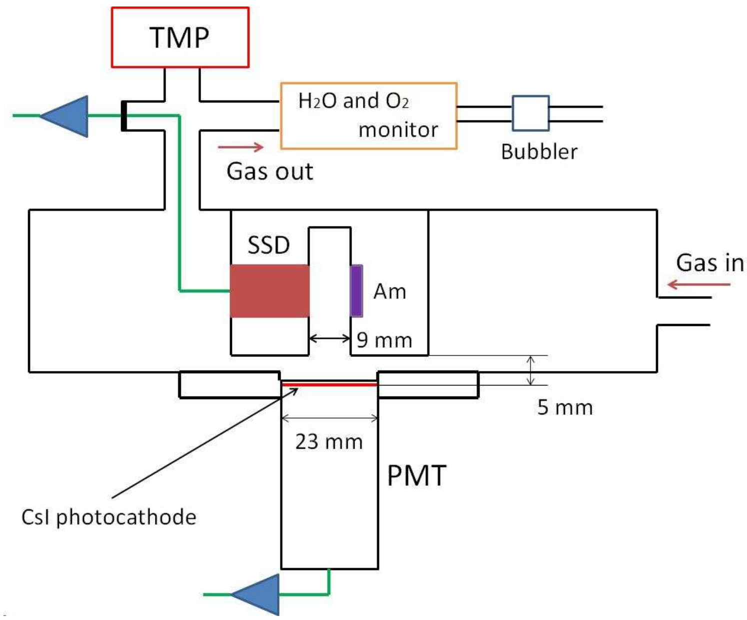

Fig. 32: The chamber for measurement of the flux of cube. the distance between the collimation hole and PMT photocathode is $\sim$ 5mm, which ensures that all photons through the collimation hole reach a photocathode of the PMT.

absolute number of photons in our acceptance N_γ is then given by

$$N_\gamma = N_{tot} * A * E_{loss} \tag{9}$$

where A is geometric acceptance in our measurement and E_{loss} is a mean energy loss of a alpha particle in CF_4. The geometric acceptance is estimated with toy Monte Carlo simulation, which gives the geometric acceptance of 3.03 %. Thus a value of the photon yield is estimated to 32.7 $\pm$ 1.6. However, this measurement have large systematic uncertainties due to geometrical configuration and we develop the next method.

5.3.2 Probability of $P(0)$

A second method is also employed to determine the number of photoelectrons produced on the photocathode of the PMT3. We take the ratio of events triggered by the SSD which leave no detected light in the PMT ($P(0)$) to the total number of events within the ADC spectrum of the PMT. It is widely known that the number of photoelectrons detected by the PMT follows Poisson distribution $P(X = k) = \frac{\lambda^k e^{-\lambda}}{k!}$ and thus we can use the Poisson relation $< N_{p.e.} >= \lambda = -\log(P(0))$ to determine the average number of primary photoelectrons. A ADC spectrum of the PMT is shown in Fig. 34 and events producing no detected light make a peak as a pedestal. We estimate the number of the inefficient events by fitting the convolution of a Gaussian and a linear function to the ADC spectrum of around the pedestal. We employed two calculation methods to determine the number of no light detected events. One method uses a value of $\frac{N}{w}$ where N is the normalization factor of

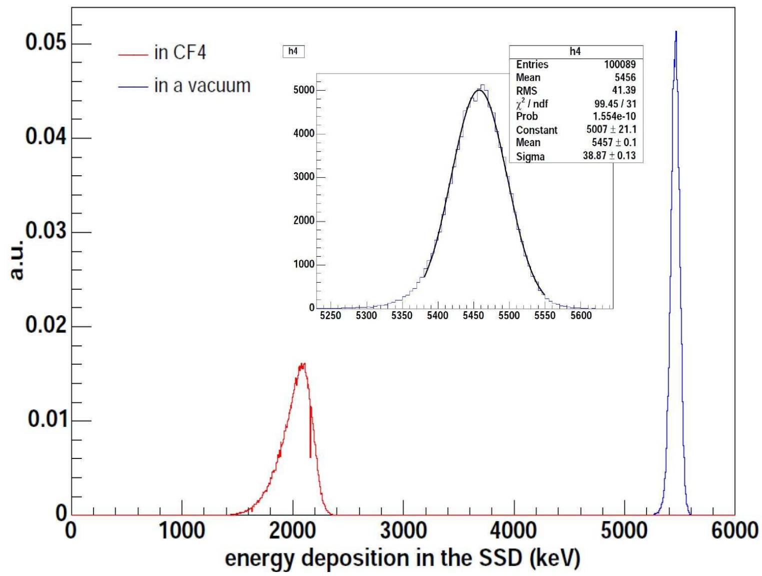

Fig. 33: ADC spectrum of the SSD, which corresponds to the energy deposition of alpha particle in the SSD. The inert is an expanded view of the high signal part of the panel. The Black line represents the fit with a Gaussian.

	QE at 160 nm	$N_{p.e.}$	N_γ
PMT3	0.0711	3.91 ± 0.02	56.2 ± 0.3
PMT4	0.0665	4.00 ± 0.02	54.1 ± 0.3

Table 5: The photon yield of scintillation cube measured with $P(0)$ method.

the fit and w is the bin-width of the histogram, since if no light detected events follow the Gaussian $\frac{\mathrm{N}}{\mathrm{w}}$ is expected to correspond to the number of the events. The other method is counting the number of the events which are above the extrapolated red line, which can be seen in Fig. 34. The value of $\mathrm{N_{p.e.}}$ determined using the first method yield a value of 3.91 ± 0.02, and the second method gives a value of 3.88 ± 0.02. The discrepancy between the two results were within the statistical error and we finally employed the first method. The photon yield N_γ is given by

$$\mathrm{N}_\gamma = \frac{\mathrm{N_{p.e.}}}{\mathrm{QE_{PMT}(160nm)}} \tag{10}$$

where $\mathrm{QE_{PMT}}$(160 nm) is the QE of the PMT at 160 nm. To estimate the systematic error of this measurement, we exchange the PMT3 for PMT4 which is the same CsI photocathode PMT as the PMT3. The results of this $P(0)$ method are summarized in Table. 5 and the statistical errors are estimated with a binomial distribution. The two results (PMT3 and PMT4) differ by more than their statistical errors, and the difference was taken to be a measure of the systematic error between two PMTs. A simple non-weighted average was therefore taken as the best estimation of N_γ, and an estimate of the total error was taken to be half of the difference between the two value, giving

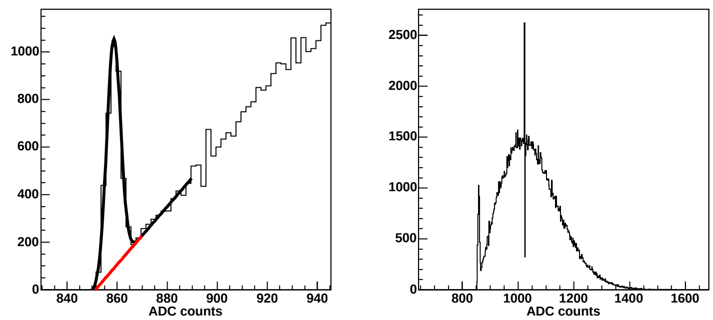

Fig. 34: ADC spectrum of the PMT. The left panel is an expanded view of the low signal part of the right panel. The black line represents the fit with a convolution of Gaussian and linear function and the red line represents the extrapolation of the linear function.

	T (μm)	hole shape	A (μm)	B (μm)	pitch (μm)
CERN GEM	50	double-conical	70	50	140
SciEnergy-50	50	cylindrical	70	70	140
SciEnergy-100	100	cylindrical	70	70	140

Table 6: General features of the GEMs where T is the thickness of the insulating foil, A is the hole diameter in electrode and B is the hole diameter in insulating foil.

$N_\gamma = 55.2 \pm 1.1$.

5.3.3 Determination of the Photon Yield

The value of N_γ determined using the energy deposition yield a value of 32.7 $\pm$ 1.6, whereas the $P(0)$ method give a value of 55.2 $\pm$ 1.1. The two results completely differed by more than their errors. We finally employ the value of the $P(0)$ method since the scintillation light can reflect on the surface of the cavity and reflected light isn't taken into account for our acceptance calculation.

5.4 Transport Efficiency

We measure the TE for various GEMs to optimize a configuration of GEM foils. Previously mentioned, investigating the parameters affecting the photoelectron collection efficiency for the HBD is main concern in this section and the TE can be improved by our effort. The TE is expected to depend mostly on the electric field in the vicinity of a GEM hole, and the electric field in the vicinity of a GEM hole depends on the hole diameter, the distance between holes, the thickness of a thin insulating foil and the voltage configurations. We measure the TE in various GEMs and the general features of the GEMs are summarized in Table. 6 and cross section of GEMs is shown in Fig 35.

A sketch of the experimental setup are shown in Fig. 31. A chamber consists of a triple GEM stack, the scintillation cube and square pad readout and is sealed by MgF_2 window to perform the absolute

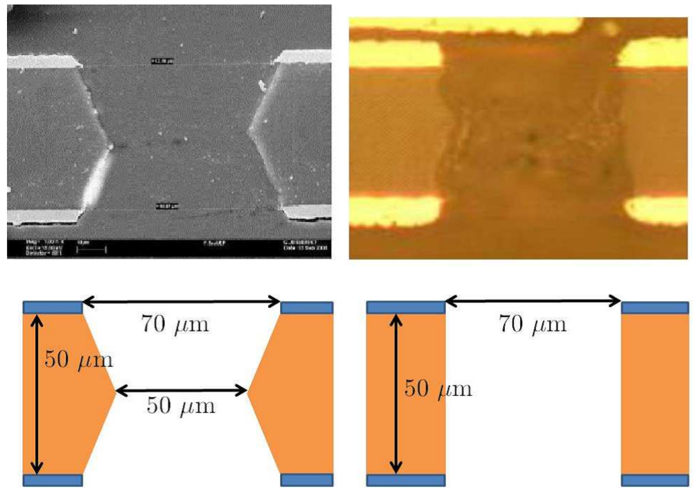

Fig. 35: Cross section of GEMs. The right panels shows a cross section of SciEnergy-50. The left panels shows a cross section of CERN GEM.

QE measurement together. The size of the square pads is 10 mm and the total number of pads is 25 in the chamber. We perform measurements with a triple GEM stack to achieve high gain. The photoelectron we finally collect in this measurement are approximately 4 to 5 while typical noise level corresponds to 0.3 e with an effective gain of 10000, which is achieved in our measurement. The effective gain in each pad is determined from an analysis of a pulse height spectrum which is obtained with a ^{55}Fe X-ray source. Fig. 36 shows a typical pulse height spectrum of the ^{55}Fe. The peak corresponds to 110 primary electrons produced by the 5.9 keV X-ray in pure CF_4 and the histogram is fitted with a convolution of Gaussian and linear function. The primary electrons often spread over multiple pads since the readout pads relatively small, and this can be seen as a slope in Fig. 36. The gas gain is monitored periodically throughout the course of each of the measurements and is found to vary by a maximum of approximately $\pm$ 3 %.
The number of collected photoelectrons is determined from an analysis of a pulse height spectrum. The observed spectrum originates from a primary photoelectron distribution which follows Poisson distribution, then it is convoluted with Polya distribution representing the gain fluctuations of the GEM detector and with a Gaussian pedestal distribution. The Polya distribution is given by

$$P(Q) \propto \frac{(1+\theta)^{1+\theta}}{\Gamma(1+\theta)} \left(\frac{Q}{\bar{Q}}\right) \exp\left[-(1+\theta)\left(\frac{Q}{\bar{Q}}\right)\right] \tag{11}$$

where θ is a parameter of the Polya distribution, $\bar{Q}$ is the mean number of electrons in avalanche and Q is the number of electrons in avalanche. The shape of the Polya distribution is described in [28], and the value of the Polya parameter θ was approximately 0.4 in our analysis. The Polya parameter θ is a free parameter of fitting, however it only weakly influences the determination of the number of primary photoelectrons using this analysis (e.g., changes in θ on the order of 20% alter the value of photoelectrons by only a few percent.).
We finally defined the transport efficiency (TE) as the ratio of the number of photoelectrons ($N_{p.e.}$)

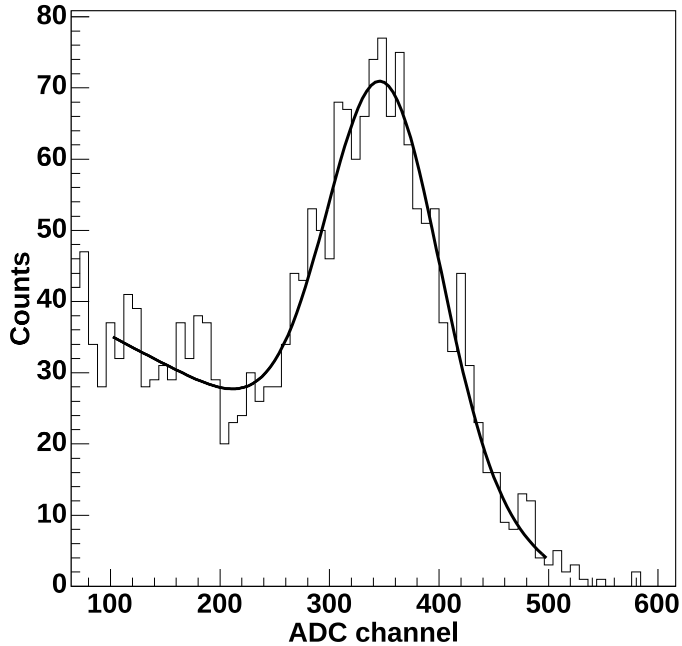

Fig. 36: Pulse height spectrum of the ^{55}Fe source used to calibrate a gain of the GEM. The peak corresponds to 110 primary electrons produced in CF_4. The solid line represents a fit of the data with a convolution of a Gaussian and a linear function.

that are estimated by fitting of the histogram discussed above to the number of photoelectrons that are successfully extracted from a CsI photocathode. It is given by

$$\epsilon_{\mathrm{TE}} = \frac{\mathrm{N_{p.e.}}}{\mathrm{N}_\gamma * \mathrm{QE_{CF_4}} * \mathrm{T_{mesh}} * \mathrm{T_{GEM}}} \tag{12}$$

where N_γ is the photon yield of the scintillation cube at 160 nm, $\mathrm{QE_{CF_4}}$ is the absolute QE of CsI photocathode measured in CF_4 at 160 nm, $\mathrm{T_{mesh}}$ and $\mathrm{T_{GEM}}$ are the mesh and GEM optical transparencies respectively.

5.4.1 Transport Efficiency of GEMs

To compare the TE of GEMs with each other, we show the various voltage dependence of the TE at first. We investigate the effect of the bias field, the field in GEM holes and in the first transfer gap on the TE. These are studied by measuring $\mathrm{N_{p.e.}}$ as a function of the applied voltage across the drift gap, the CsI-coated GEM and the first transfer gap. This efficiency is proportional to the total number of photoelectrons collected by a GEM. Fig. 37 shows the TE as a function of bias field. We perform measurements with the same voltage configuration for red circles and blue squares, both of them are 50 μm thickness GEM. Green triangles can't be compared directly with the 50 μm GEMs since the applied voltage across the GEM is different for the SciEnergy-100. However, the applied

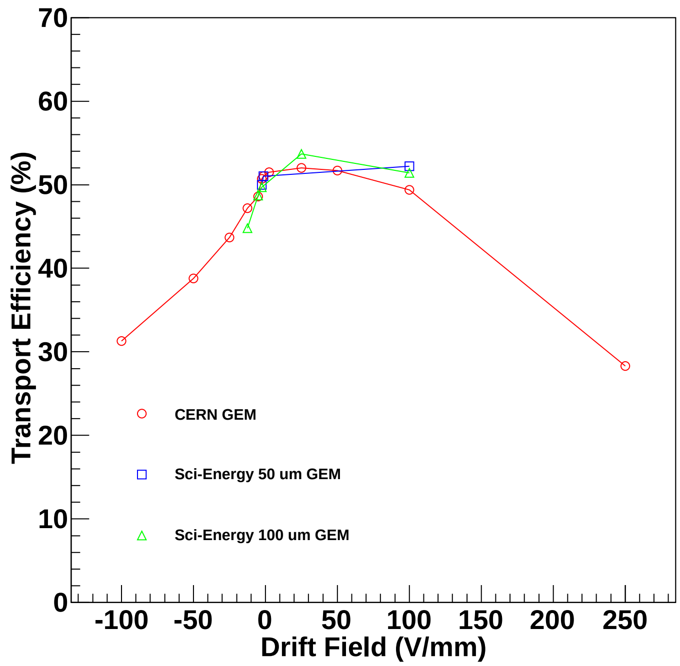

Fig. 37: Photoelectron transport efficiency vs. applied drift field. Red circles represents measurement with a CERN GEM, blue squares represent measurement done with a SciEnergy-50 and green triangles represent measurement done with SciEnergy-100.

voltage in the 1st transfer gap is the same in these plots. Fig. 37 shows a plateau for moderate positive drift fields (forward bias), and decreases for negative drift fields (reverse bias) and large forward bias (see section 3.2 for forward bias and reverse bias). The decrease for reverse bias means that more photoelectrons are pulled toward the mesh with increasing reverse bias. The decrease for large forward bias means photoelectrons are strongly accelerated toward the GEM surface and then absorbed by the CsI photocathode again. All plots show the peak at a positive drift field, however the HBD operates at a slightly negative drift field (typically ∼50 V/cm). This voltage configuration introduces some additional loss in the transport efficiency. CERN GEM and SciEnergy-50 show the same absolute transport efficiency and this indicate that the hole shape doesn't affect the transport efficiency. It should be noted that even if the absolute transport efficiency is the same between CERN GEM and SciEnergy-50, we can expect that CERN GEM can collect more photoelectrons due to its larger active area of CsI photocathode since CsI can be evaporated in the taper of the insulating foil.
The value of T_{GEM} reflects this effect and the value of T_{GEM} is 0.81 for CERN GEM [17] and 0.77 for SciEnergy-50 and SciEnergy-100. The other dependence are shown in Fig. 38. The transport efficiency is slightly affected by electric field in the transfer gap. Therefore, we can say that at the assumed voltage configuration of the transfer gap (300-500 V/mm) the transport efficiency of CERN GEM, SciEnergy-50 and SciEnergy-100 is unaffected by electric field in the transfer gap.

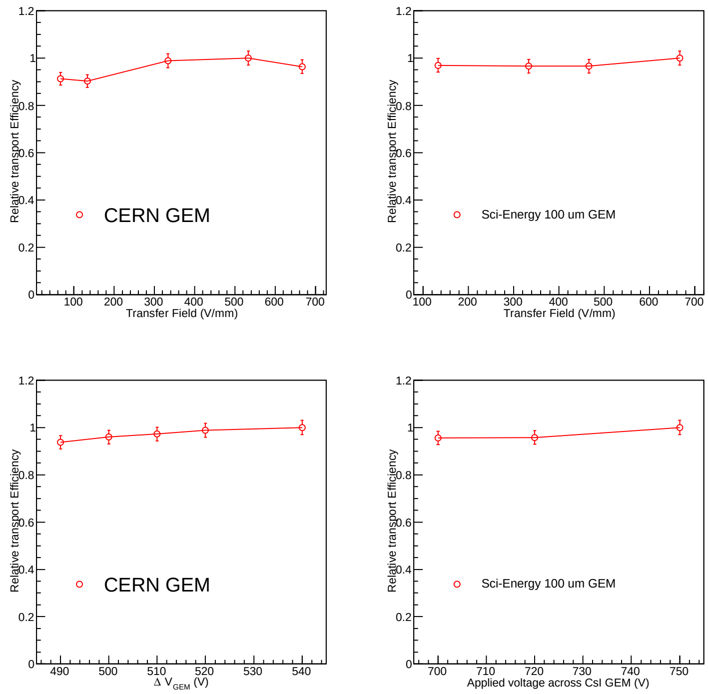

Fig. 38: Relative transport efficiency vs. applied voltage. The upper panels shows the relative transport efficiency versus voltage across the first transfer gap with the voltage across the GEM held constant and the lower panels shows the relative transport efficiency versus voltage across the GEM with the reverse bias (2.5 V/mm). Each transport efficiency are normalized to the median of the largest value in each measurement.

Furthermore, we can say that within the error which is originated from gain calibration the transport efficiency doesn't change with the applied voltage across the GEM.
However, As mentioned previous section, higher gain of the top GEM can reduce the relative amount of the ionization electrons generated in the first transfer gap. Therefore, the applied voltage across the top GEM play an essential role in performance of the HBD even if it doesn't change the transport efficiency.

5.4.2 Obtained Results and Remarks

In previous subsection, we show the various relations between the transport efficiency and voltage configurations, however there are very little correlation between them. Thus, we determined that the value of ϵ_{TE} in a typical voltage configuration is taken as a representative value. The typical configurations are shown in Tab. 7. The representative value is 0.51 ± 0.03 for CERN GEM and SciEnergy-50 and 0.52 ± 0.03 for SciEnergy-100. The error of these values include the error of the absolute QE at 160 nm, the photon yield and the number of collected photoelectrons which is mainly caused by the gain calibration. These values are summarized in Table 8. All results agree within the error. By combining the assumption that the transport efficiency is a function of the strength

	Drift field (V/mm)	V_{GEM} (V)	Transfer gap (V/mm)
CERN GEM	Reverse bias 2.5	500	333
SciEnergy-50	Reverse bias 2.5	500	333
SciEnergy-100	Reverse bias 2.5	750	333

Table 7: Typical voltage configurations for CERN GEM, SciEnergy-50 and SciEnergy-100.

	T_{mesh}	T_{GEM}	QE (%)	N_γ	$N_{p.e.}$	ϵ_{TE}
CERN GEM	0.885	0.81	23.0 ± 0.5	58.4 ± 1.2	5.0 ± 0.1	0.52 ± 0.03
SciEnergy-50	0.885	0.77	23.3 ± 0.5	57.9 ± 1.1	4.69 ± 0.08	0.51 ± 0.03
SciEnergy-100	0.885	0.77	9.6 ± 0.2	55.2 ± 1.1	1.89 ± 0.04	0.52 ± 0.03

Table 8: Various parameters to calculate the transport efficiency. The absolute QE of the 100 μm GEM is very low since it was exposed to air a little bit longer than usual. The value of the photon yield in CERN GEM is larger than previously mentioned since the position of the SSD in the cube changed by an accident and we measured the photon yield again with the same method.

of the surface electric field and the fact that all results agree within the error, we conclude that the transport efficiency mostly depend on the ratio of the hole diameter to the distance between holes and slightly depend on voltage configurations.

6 Gas Transmission

Vacuum Ultra Violet photons are produced in a radiator of the HBD as a Čerenkov photon, and travel toward a CsI photocathode. However, there is absorption of the UV photons due to CF_4 gas itself and impurities. UV photon absorption of CF_4 inevitably takes place and thus we should consider it as an intrinsic loss of photons. Absorption caused by any impurities such as oxygen and water can be avoidable to some extent. In this section, we explain the transmission of CF_4 and impurities.

6.1 CF_4 Transmission

Absorption in CF_4 is reported in [17] and the result is illustrated in Fig. 39. Fig. 39 shows a loss

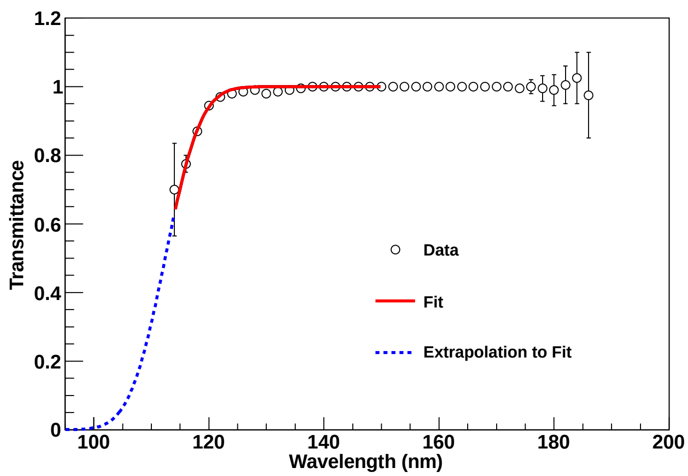

Fig. 39: VUV transmission spectra for a 510 mm gas volume.

of VUV intensity in CF_4 for a 510 mm gas volume over a wavelength range from 114-184 nm and the data was fitted with Error Function which is given by

$$\mathrm{erf}(x) = \frac{2}{\sqrt{\pi}} \int_0^x e^{-t^2} dt \tag{13}$$

The dotted blue line is a extrapolation to fit and the transmittance goes to zero at approximately 100 nm (12.4 eV). By extrapolating the data, we assumed the transmission of CF_4 in photon energy above 10.3 eV where the Čerenkov photon yield and QE of CsI relatively high.This result overestimates the loss of the Čerenkov photons in CF_4 since Čerenkov photons produced near the CsI photocathode don't travel over 510 mm. However, the photon interaction cross section with CF_4 below 130 nm differ by experimental group and thus this overestimation is valid. The value of the photon interaction cross section with CF_4 is shown in Appendix.

6.2 Water and Oxygen Transmission

High gas purity is a crucial factor for performance and operation of the HBD. In particular, impurities such as water vapor and oxygen affect the total produced number of photoelectrons. Both water vapor and oxygen have strong absorption peaks for Čerenkov light in the spectral range of sensitivity of the CsI photocathode, and even small levels of either of these contamination can produce a significant loss of photoelectrons. This is illustrated in Fig. 20, which shows the photon interaction cross section for water and oxygen in the wavelength range of sensitivity of CsI photocathode. Fig. 40 and Fig. 41 show how this translates into a loss in the number of the Čerenkov photons in a 500 mm long radiator. These figures are calculated using the data points from [21] which are performed

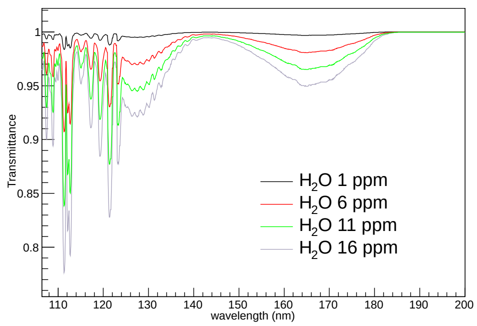

Fig. 40: Transmittance of light. This panel shows a loss of light caused by water

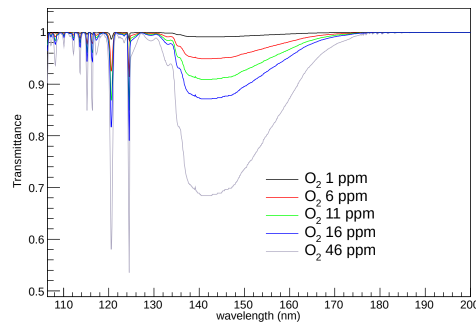

Fig. 41: Transmittance of light. This panel shows a loss of light caused by oxygen.

over almost full wavelength range of our interest and the transmissions T are given by

$$T = \exp(-\frac{L}{\lambda}) \tag{14}$$

where L is propagated distance of a Čerenkov photon, which depends on the produced point of the Čerenkov photon and λ is the mean free path of water and oxygen. The loss rate of photoelectrons in the HBD due to water and oxygen can be obtained with combination of absorptions caused by the impurities, intrinsic absorption of CF_4 and the absolute QE of CsI photocathode since the photoelectron yield have wavelength dependence. The absolute QE of CsI in wavelength under 120 nm (over 10.3 eV), which we didn't measure, is extrapolated under an assumption as discussed in the next section. The loss of photoelectrons over full wavelength range due to the impurities is evaluated. Fig. 42 shows the relative number of photoelectrons produced in 500 mm long radiator as a function of ppms of water and oxygen contamination in CF_4. This plot indicates that if we keep both water and oxygen levels in CF_4 less than 5 ppm the loss of photoelectrons is less than 1 %.

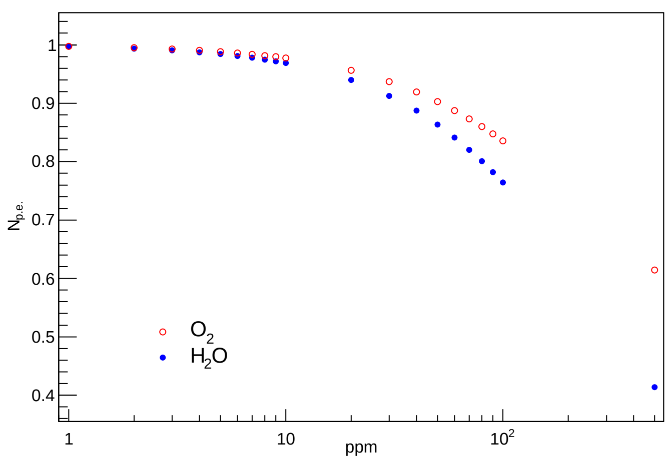

Fig. 42: Relative number of photoelectrons, $N_{\mathrm{p.e.}}$, produced in 500 mm long radiator as a function of ppms of water and oxygen contamination in CF_4. This plot includes the wavelength dependence of the photoelectron yield due to the wavelength dependence of the transmission of CF_4 and absolute QE of CsI photocathode.

7 Figure of merit N_0 and photon yield

By combining the results we obtained in laboratory test, we can guess the number of photoelectrons we observe in beam test (equivalently, the E16 experiment). In this chapter, we summarize the results which we introduced in previous chapters and show the typical expected number of photoelectrons. For simplicity, CERN GEM is treated as a representative in this chapter
The average number of photoelectrons $N_{\mathrm{p.e.}}$ in a Čerenkov counter with a radiator of length L is given by

$$\begin{aligned}
N_{\mathrm{p.e.}} &= \int_0^{\mathrm{L}} d\mathrm{L} \int d\lambda \, \frac{dN}{d\lambda d\mathrm{L}} \cdot \mathrm{QE}(\lambda) \cdot T_{\mathrm{CF}_4} &(15)\\
&= 2\pi z^2 \alpha \cdot \mathrm{L} \cdot \sin^2\theta \int d\lambda \, \frac{1}{\lambda^2} \cdot \mathrm{QE}(\lambda) \cdot T_{\mathrm{CF}_4} &(16)\\
&= \frac{2\pi z^2 \alpha}{2\pi \hbar c} \cdot \mathrm{L}/\bar{\gamma}_{\mathrm{th}}^2 \int dE \; \mathrm{QE}(E) \cdot T_{\mathrm{CF}_4} &(17)\\
&= 370.0 \cdot \mathrm{L}/\bar{\gamma}_{\mathrm{th}}^2 \int dE \; \mathrm{QE}(E) \cdot T_{\mathrm{CF}_4} &(18)\\
&= N_0^{\mathrm{ideal}} \cdot \mathrm{L}/\bar{\gamma}_{\mathrm{th}}^2 &(19)
\end{aligned}$$

where $\bar{\gamma_{\mathrm{th}}}$ is the average Čerenkov threshold over the sensitive bandwidth of the counter, N_0^{ideal} is the figure of merit of the Čerenkov counter, z is the charge number of the incident particle (we only focus on electron thus z = 1), T_{CF_4} is the intrinsic transmittance of CF_4 and θ is the Čerenkov angle. From (16) to (17) we use approximation which is valid for relativistic particles as

$$\begin{aligned}
\sin^2\theta &= 1 - \cos^2\theta &(20)\\
&= 1 - \frac{1}{\beta^2 n^2} &(21)\\
&\simeq 1 - \frac{1}{n^2} &(22)\\
&= \frac{1}{\bar{\gamma}_{\mathrm{th}}^2} &(23)
\end{aligned}$$

The ideal figure of merit, i.e. in the absence of any losses such as photon absorption due to the impurities, optical transparency of mesh and relatively low transport efficiency, is obtained by integrating the CsI absolute QE times the CF_4 gas transmittance (T_{CF_4}) over the sensitive bandwidth of the counter. The HBD is sensitive to photons between the threshold of the CsI photocathode ∼6.2 eV (∼200 nm) which is determined by the work function ϕ of CsI and the CF_4 cut-off (the 50 % cut-off point is at ∼ 11.0 eV and the transmission goes to zero at ∼ 12.4 eV).
Our absolute QE measurements are performed over the limited range (6.2-10.3 eV) due to the light intensity of the deuterium UV lamp at ∼10.3 eV, thus we extrapolate the data of Fig. 43 from 10.3 eV till the absolute QE cut-off at 12.4 eV by fitting the data with a linear function under the assumption that there is a linear dependence of the QE vs. photon energy. For T_{CF_4} we use the

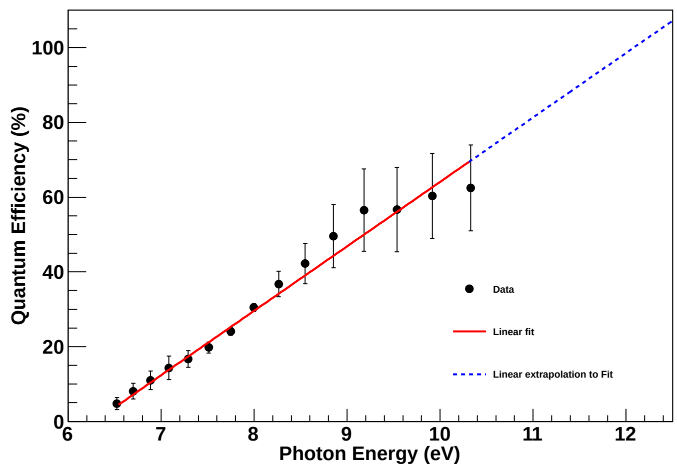

Fig. 43: Absolute QE of CsI in CF_4 over the bandwidth 6.2-10.3 eV. The data was fitted with a linear function. By extrapolating the data we guess the absolute QE above 10.3 eV.

values shown in previous chapter. We then obtain an ideal value for N_0^{ideal} of

$$
\begin{aligned}
N_0^{\mathrm{ideal}} &= 370.0 \int_{6.2\ \mathrm{eV}}^{12.4\ \mathrm{eV}} dE\ \mathrm{QE}(E) \cdot T_{\mathrm{CF_4}} \quad (24) \\
&= 732\ \mathrm{cm}^{-1}(\text{linear extrapolation}) \quad (25)
\end{aligned}
$$

In the actual Čerenkov counter, this figure gets degraded by a number of factors that reduce the overall photoelectron yield. These include the transparency of the gas due to impurities, T_{imp}, the optical transparency of the mesh, T_{mesh}, the optical transparency of the top GEM (which reduces the effective CsI photocathode area), T_{GEM} and the transport efficiency of the photoelectrons, once extracted from the photocathode, into the holes of the GEM, ϵ_{TE}. We assume these efficiencies are wavelength independent and straightforward to measure or estimate. In the following we discuss all these factors and quote their average values in Table 9.

The optical transparency of the mesh, T_{mesh}, is simply determined by the opacity of the wire mesh. 30 μm diameter wires are arranged in a lattice shape and the distance between wire centers is 508 μm. Thus we calculated it to be 88.5 %.

The optical transparency of the photocathode, T_{GEM}, gives the effective area of the CsI photocathode and is determined by the hole pattern in the GEM foil. Sci-Energy GEMs shows perfectly cylindrical holes and the hole diameter is 70 μm. The holes are arranged in triangle lattice shape with the 140 μm pitch and we thus calculated T_{GEM} to be 0.773 for SciEnergy GEMs. While the CERN GEM holes are not perfectly cylindrical and have a tapered shape that consists of an outer hole in the copper layer and an inner hole in the insulating foil. The T_{GEM} is given by [17] and they determined the value by measuring the photocathode efficiency of a solid planar photocathode and comparing it with that of a photocathode deposited on a CERN GEM foil. They report an average value for the optical transparency of the CERN GEM foil of 0.81.

The transparency of the gas due to impurities $T_{\rm imp}$ only include the absorption caused by any impurities such as oxygen and water vapor. The intrinsic transmission of the HBD gas is already included in $T_{\rm CF_4}$. $T_{\rm imp}$ is estimated to be 95 % and it is equivalent to 10 ppm of water and 10 ppm of oxygen.

The transport efficiency, $\epsilon_{\rm TE}$, for transferring photoelectrons produced on the photocathode to the holes in the GEMs was measured and described in the previous chapter. The value is given as 0.52.

With all of these losses, the expected figure of merit for each GEM is computed to be

$$N_0^{\rm calc} = T_{\rm imp} \cdot T_{\rm mesh} \cdot T_{\rm GEM} \cdot \epsilon_{\rm TE} \cdot N_0^{\rm ideal} \quad (26)$$

$$= 259\ ({\rm cm}^{-1}) \quad (27)$$

with an estimated uncertainty 7%. The uncertainty comes primarily from CF_4 transmission near its cut-off and the transport efficiency. Using the calculated average $\bar{\gamma}_{\rm th} = 28.8$ and an average radiator length of $L = 500$ mm, the expected number of photoelectrons is given by

$$N_{\rm p.e.} = N_0^{\rm calc} \cdot L/\bar{\gamma}_{\rm th}^2 \quad (28)$$

and it gives a value of $N_{\rm p.e.} = 15.6$. Expected number of photoelectrons naturally depends on quality of a photocathode and thus this result of $N_{\rm p.e.} = 15.6$ is only a typical value.

	CERN GEM	SciEnergy-50	SciEnergy-100
$N_0^{\rm ideal}$ (cm^{-1})	732	732	732
Optical transparency of mesh $T_{\rm mesh}$	0.885	0.885	0.885
Opacity of photocathode $T_{\rm GEM}$	0.81	0.773	0.773
Gas transparency due to impurities $T_{\rm imp}$	0.95	0.95	0.95
Transport efficiency	0.52	0.51	0.52
$N_0^{\rm calc}$ (cm^{-1})	259	243	247
$N_{\rm p.e.}$ expected	15.6	14.6	14.9

Table 9: Figure of merit and Čerenkov photon yield. We assume that CsI photocathode of each GEM shows the same QE.

8 Beam Test

The HBD is characterized by its insensitivity to hadrons, i.e. by a large hadron rejection factor while keeping a high electron detection efficiency. In order to characterize and quantify both the hadron rejection factor and the electron detection efficiency, we performed beam tests two times at J-PARC K1.1BR test beam-line. In this chapter, evaluated properties are shown at first, and then the experimental setups and results of each beam test are discussed.

8.1 Evaluated Properties

Required property for the HBD is a hadron rejection factor of 100 with an electron detection efficiency of 70%. The hadron blindness of the HBD is achieved by operating the detector in the reverse bias field as previously mentioned. The drift field E_{D} manipulates the collection efficiency of both photoelectrons and ionization electrons. The collection efficiency of photoelectrons measured as a function of E_{D} is studied with the scintillation cube described in previous chapter. We thus need to understand the number of ionization charge deposited by a charged particle as a function of the drift field to search for optimum operation point. We performed measurements as a function of the drift field at J-PARC K1.1BR with a 1 GeV/c beam of negative particles (mainly pions) containing a few tens of percent of electrons. Results of each beam test named T43 and T47 are briefly summarized below.

- T43

  T43 beam test shows very poor hadron rejection factor due to very low gain of the top GEM. However, the number of photoelectrons are in good agreement with expected value from laboratory test. The MPV of photoelectron we measured in T43 is $\sim$12 e and the expected value from laboratory results is 13.5 $\pm$ 1.0 e.

- T47

  To increase the gain of the top GEM and the number of photoelectrons, we produced new GEMs. We observe 7 photoelectrons and achieve a hadron rejection factor of 100 with electron detection efficiency 70 %.

The following sections mainly focus on T47 and results of T43 are briefly described.

8.2 Results of T43

T43 beam test are held at J-PARC K1.1BR to measure a hadron rejection factor and the number of photoelectrons. We prepared three setups for T43 and all of them consist of a double GEM stack and the pad readout. The pad readout consists of hexagonal pads and the side length of the pads is 17 mm, which is almost the same size as the Čerenkov blob size. Therefore both electrons and pions produce single hit pad if they hit at center of the pad. T43 is the first beam test where we use hadron beams for the HBD. A large part of the GEM we prepared for T43 frequently discharge and eventually show dead short. We can take only one calibrated data-set in entire beam time. Calibration is done with 5.9 keV X-ray from ^{55}Fe.
The setup of the HBD for this data-set is shown in 44 and the measured pulse-height spectra with electrons and pions in reverse bias mode are shown in Fig.45.

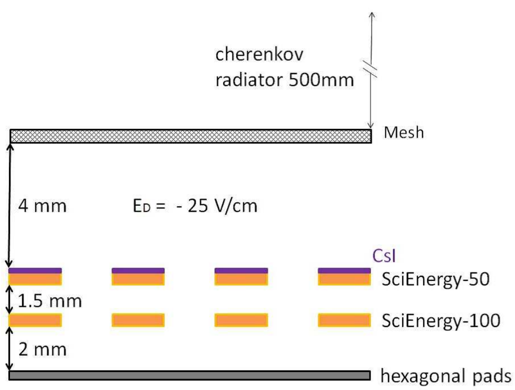

Fig. 44: Setup of the HBD in T43. ^{55}Fe is used for a determination of the gas gain of the GEM. Each GEM is directly powered by HV module without resistor chain.

A hadron rejection factor derived from the pion spectrum is shown in Fig. 46. Hadron rejection factor of the order of 10 is achieved with an amplitude threshold of $\sim$20 e. This small rejection factor is due to the very large Landau tail of pions, whose MPV is 1.9 e. This large Landau tail is caused by low gain of the top GEM. The collection of ionization charge produced in the transfer gap (between the top and the bottom GEM) is subject to a only 1-stage amplification, however if the gain of the top GEM is low, this ionization charge can leave relatively large signals which is comparable to that of Čerenkov photons. This significantly affect the performance of hadron blindness.
The ionization charge in the transfer gap (1.5 mm) with 1GeV/c pions can be calculated and is given by approximately 16 e while the gain of the top GEM in T43 is $\sim$7. We can expect that the signal on the readout includes the large amount of ionization charge produced in the transfer gap.
The number of photoelectrons can be calculated by subtracting the ionization charge produced in the drift gap and transfer gap from primary charge we measured in reverse bias mode.

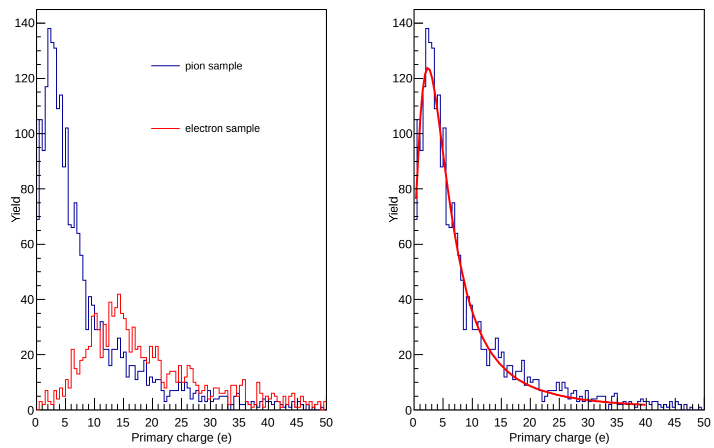

Fig. 45: Pulse-height spectra measured with 1 GeV/c pions and electrons. The solid line in the right panel represents a fit to a Landau distribution of the measured spectrum of pions. The left panel is an overplot of the measured spectra of pions and electrons.

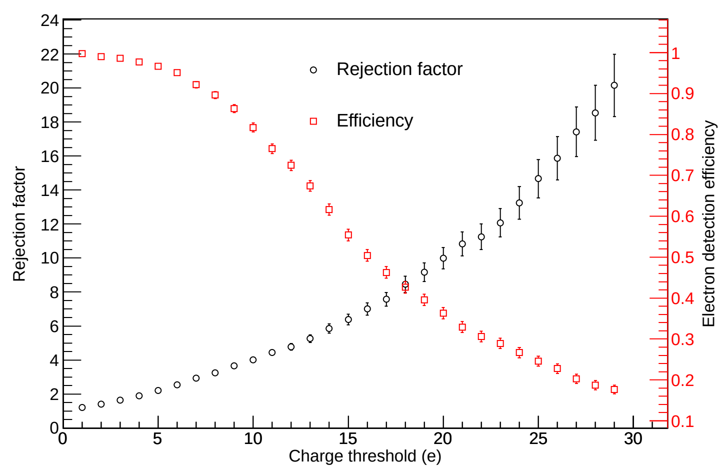

Fig. 46: Hadron rejection factor derived from the pion pulse-height spectrum as a function of the amplitude threshold in units of the primary charge. The error bars represent the statistical errors.

The ionization charge with 1 GeV/c electrons in reverse bias mode can be obtained by using the ratio of the ionization charge with electrons in forward bias mode to the ionization charge with pions in forward bias mode. The measured pulse-height spectra with electrons and pions in forward bias are shown in Fig. 47. These spectra are obtained without photocathode.

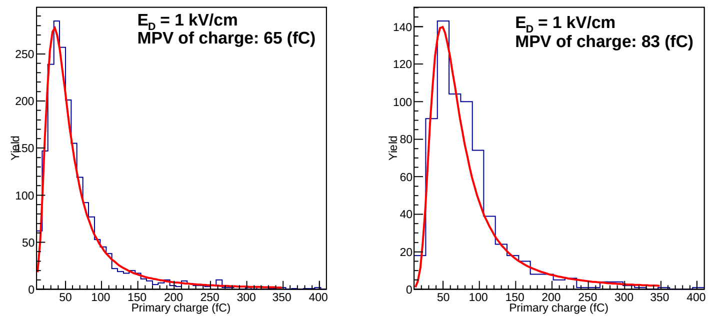

Fig. 47: Pulse-height spectra measured with 1 GeV/c pions and electrons in forward bias mode. The spectra are measured with GEM of no photocathode. The right panel is measured with electrons and the left panel is measured with pions. The solid lines represent fits to a Landau distribution of the measured spectra.

The ratio is given by 1.3 and this value is in good agreement with the calculated value from the Bethe-Bloch formula. the ionization charge with pions in reverse bias mode is 1.9 e, thus the ionization charge with electrons is expected to be $1.3 \times 1.9 = 2.5$ e. The MPV of the primary charge with 1 GeV/c electrons in reverse bias mode is $\sim$ 14.5 e shown in Fig. 45. Therefore the number of photoelectrons we measured in T43 is $\sim$12. The QE of the CsI photocathode used in T43 was measured in advance and gives a value for $N_0^{\mathrm{calc}} = 224$. The expected number of photoelectrons is 13.5 $\pm$ 1.0 and this result indicates that our assumption about linear extrapolation of QE and various results of laboratory tests are valid. The results of T43 are summarized below

- a hadron rejection factor of 10 and an electron detection efficiency of 35 % with an amplitude threshold of $\sim$20 e are obtained which is not satisfactory.

- we observe 12 photoelectrons in T43 and the value is in good agreement with the expected value from laboratory tests.

- a large part of the GEM show dead short by hadron beam and only one calibrated data-set is taken, however the gain of the top GEM is very low ($\sim$7).

8.3 Overview of T47

T47 beam test are held at J-PARC K1.1BR to measure a hadron rejection factor and the number of photoelectrons. To overcome the results of T43, we produced two kinds of new GEMs shown in Table 10.

	T (μm)	hole shape	A (μm)	B (μm)	pitch (μm)
Raytech-A	50	double-conical	55	30	240
Raytech-B	50	double-conical	55	30	110

Table 10: General features of new GEMs where T is thickness of the insulating foil, A is hole diameter in electrode and B is hole diameter in insulating foil.

The insulating foil of these GEMs are made of kapton which is a polyimide film developed by DuPont while the insulating foil of SciEnergy-50 and SciEnergy-100 used in T43 are made of Liquid Crystal Polymer (LCP).
All new GEMs have the smaller hole diameter in both electrode and insulating foil than those of the CERN GEMs, SciEnergy-50 and SciEnergy-100 to achieve larger gain. Raytech-A is used as the top GEM since The effective area of Raytech-A is ∼90%. If we assume the transport efficiency is the same between the GEMs used in T43 and Raytech-A, the number of photoelectrons increases by 15 %. The size of the new GEMs is 50 × 50 mm^2 and this is sufficiently larger than the Čerenkov blob size.
In T47, we performed systematic measurements as a function of the drift field to search for the optimum operation point.

8.4 Setup of T47

The test setups of T47 is shown in Fig. 48.

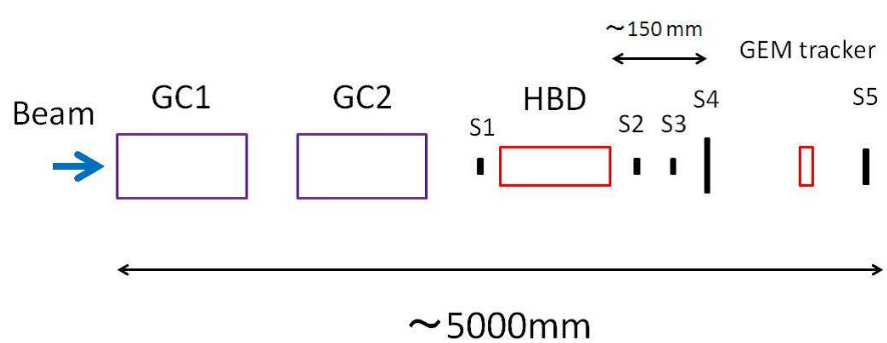

Fig. 48: Setup of T47.

Five Scintillators, two gas Čerenkov detectors and the HBD are aligned along the beam line at J-PARC K1.1BR. A coincidence of S1,S2,S3 and S5 is used as a beam trigger. Two gas Čerenkov detectors are used to identify electrons and pions. These gas Čerenkov detectors are filled with compressed dry air and only electrons can emit the Čerenkov light. Scintillator S4 is used to reduce multiple-hit events. Table 11 summarizes the sizes of scintillators.

S1	S2	S3	S4	S5
10	10	10	100	50

Table 11: Size of each scintillator (mm)

8.5 Setup of the HBD

The HBD for T47 consists of a triple GEM stack and a pad readout shown in Fig. 49.

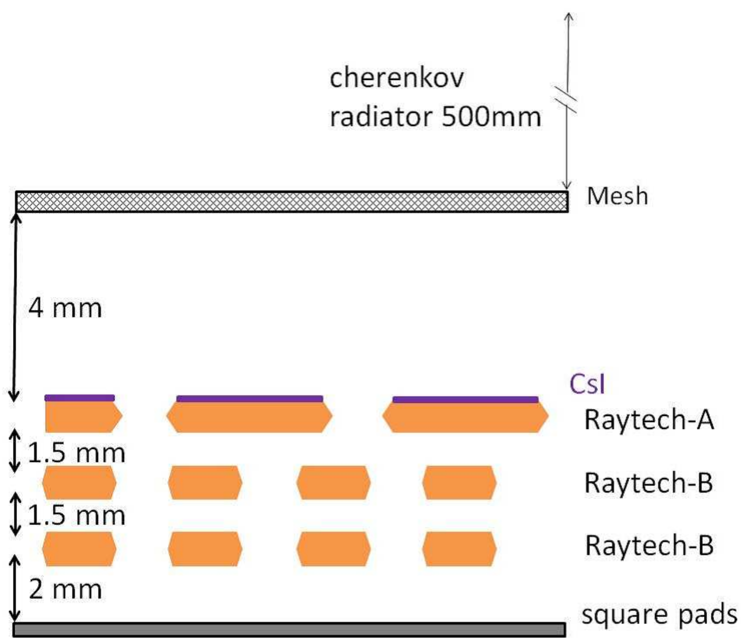

Fig. 49: Setup of the HBD. ^{55}Fe is used for a determination of the gas gain of the GEM. Each GEM is directly powered by HV module without resistor chain.

The pad readout consists of square pads and the side length of the square pads is 10 mm resulting in 25 pads in the detector. This pad size is smaller than the Čerenkov blob size (radius of 17 mm) and this may degrade the Signal-to-Noise ratio, however it doesn't matter due to very high gain of new GEMs in T47. Effective gain in T47 is approximately 20000 while the noise level of each pad is $\sim$500 e. Pions produce single pad hits whereas electrons most probably produce multiple-pad hits thereby providing an additional powerful handle on the hadron rejection.

8.6 Spectra of Scintillators and Gas Čerenkov detector

The acquired spectra of the scintillators are shown in Fig. 50. S4 is 100 $\times$ 100 mm^2 scintillator used to reduce multiple-hits events and Fig. 51 shows the number of hits in a event. Single hit events are approximately 40 % of all events. We assume that all particles which pass through the sensitive area of the HBD always leave signals in S4 and thus we require S4 is single hit for analysis data. The acquired spectra of gas Čerenkov detectors are shown in Fig. 52. Electrons can emit the Čerenkov light in GC1 and GC2 while pions leave no signal. With spectra of GC1 and GC2, we can distinguish electrons and pions from charged particle and we define electron sample as an event of GC1 $>$ 200 and GC2 $>$ 200 while pion sample as an event of GC1 $<$ 110 and GC2 $<$ 90.

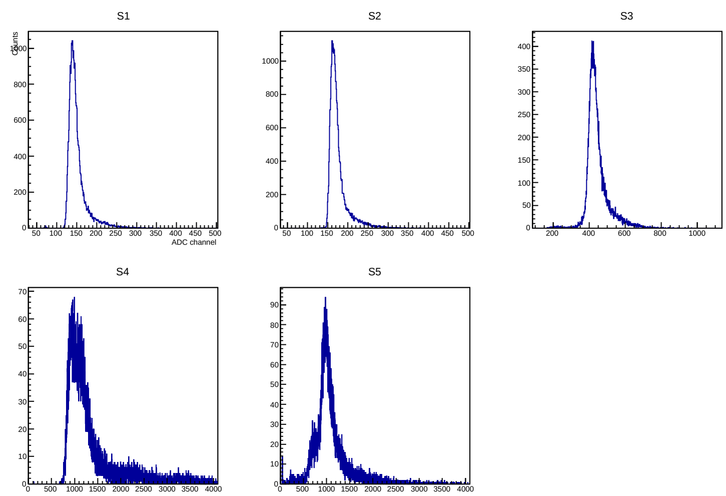

Fig. 50: ADC spectra of scintillators. The Landau distribution can be seen.

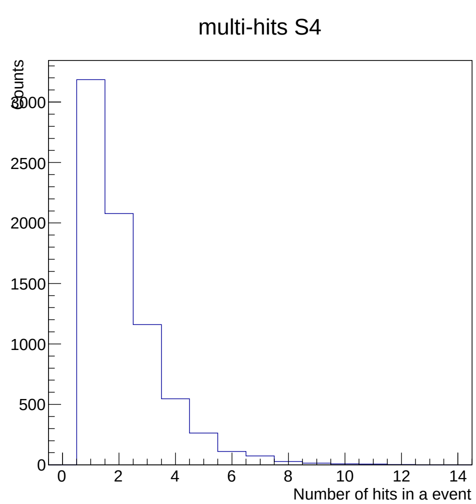

Fig. 51: The number of S4 hits in a event.

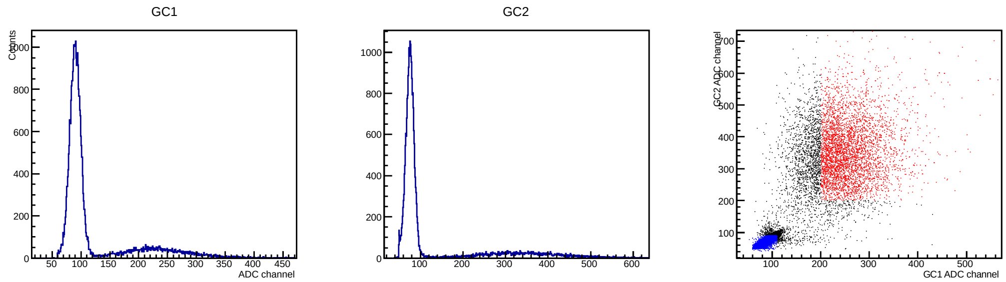

Fig. 52: ADC spectra of gas Čerenkov detectors and scatter plot of GC1 vs GC2. We distinguish electrons and pions from charged particles by determining the threshold value in the spectra. In the right panel, red points represent electrons and blue points represents pions.

8.7 Analysis method

To calculate a hadron rejection factor, we use the hit size information as well as primary charge threshold. The analysis procedure consists of the following steps:

1. Raw ADC values of each pad in pedestal run are fitted with a Gaussian. We define the mean of a Gaussian as Mean$[i]$ and the sigma of a Gaussian as $\sigma[i]$ where i is pad number.

2. We define a fired pad as a pad which have ADC value larger than the pedestal by $3\sigma[i]$. If ith pad is fired, the ADC value of ith pad (ADC$[i]$) satisfy a equation below

$$\mathrm{ADC}[i] - \mathrm{Mean}[i] > 3\sigma[i] \tag{29}$$

3. If the number of fired pads around a pad with maximum charge ($\mathrm{N_{fired}}$) is more than two, we define this events as a survived event (cluster size analysis). $\mathrm{N_{fired}}$ is shown in Fig. 53. The most probable value of $\mathrm{N_{fired}}$ with electrons is 3 or 4 while that of pions is 0. This indicates the ionization charge is localized in one pad and electrons with Čerenkov photons fire a few pads around the pad with maximum charge.

4. Total charge in an event is determined as the sum of the fired pads around a pad with maximum charge and the pad with maximum charge. Total charge calibrated with ^{55}Fe is shown in Fig. 54.

5. The rejection factor is defined as the ratio of the number of events determined by GC1, GC2 and S4 to the number of events over the amplitude threshold in the survived events.

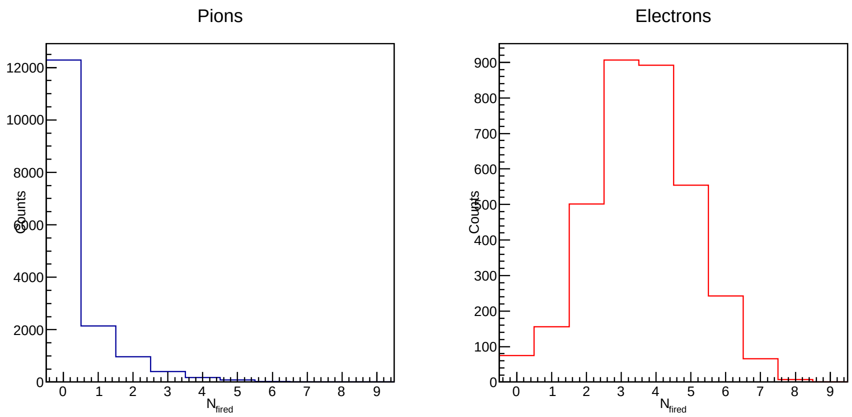

Fig. 53: The number of fired pads around a pad with maximum charge. The right panel is measured with electron samples and the most probable number is 3 or 4 while that of pion samples is 0.

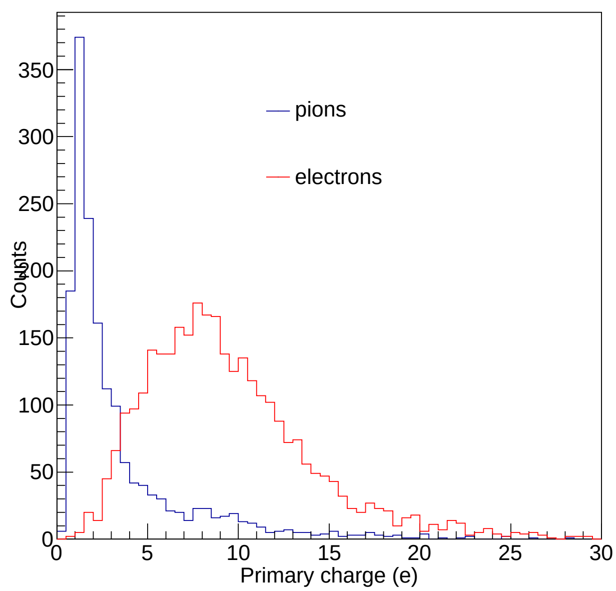

Fig. 54: Pulse-height spectra measured with 1 GeV/c pions and electrons at $E_{\mathrm{D}} = -12.5$ V/cm. These spectra are the sum of the maximum charge pad and the fired pads around the maximum pad.

8.8 Number of Photoelectrons

The number of photoelectrons can be calculated as T43 and estimated at $E_{\mathrm{D}} = -12.5$ V/cm. The MPV of primary charge of pions in Fig. 54 is larger than the real value due to threshold effect. Triggered particles pass through the center of the readout pads and thus the sum of the charge in the central 9 pads is used to estimate the MPV of the primary charge of pions and electrons. That sum is shown in Fig. 55 and the MPV of pion is 0.2 e. It gives the MPV of the ionization charge of electrons 0.3 e. By subtracting the ionization charge of 0.3 e from the spectrum shown in Fig. 55, the number of photoelectrons is $\sim$7. The number of photoelectrons we measure in T47 is smaller than we expected and this is considered to be due to smaller transport efficiency of the top GEM compared to that of regular GEM.

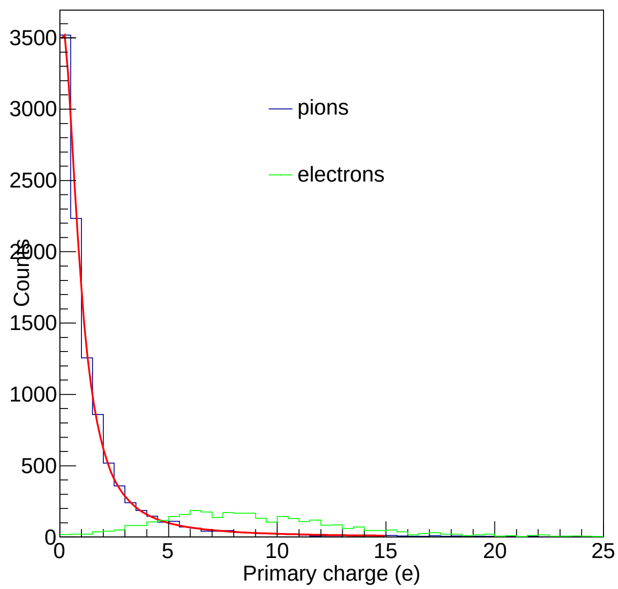

Fig. 55: Pulse-height spectra measured with pions and electrons at $E_{\mathrm{D}} = -12.5$ V/cm. The red line represent a fit of pion spectrum with a Landau distribution.

8.9 Hadron Rejection Factor

The hadron rejection factor derived from the pion spectra obtained at various value of the drift field E_{D} is shown in Fig. 56. The applied voltage across the top GEM is 500 V. The rejection is limited by the long Landau tail and depends on the amplitude threshold. As E_{D} increases, Rejection factor rapidly increases and seems to go to plateau around $E_{\mathrm{D}} = -50$ V/cm. This is because the primary charge with pions around 0 e increases as E_{D} increases and Fig. 57 shows the primary charge of pion samples. Thus we can expect that the optimum operation point is $E_{\mathrm{D}} = -75$ V/cm.

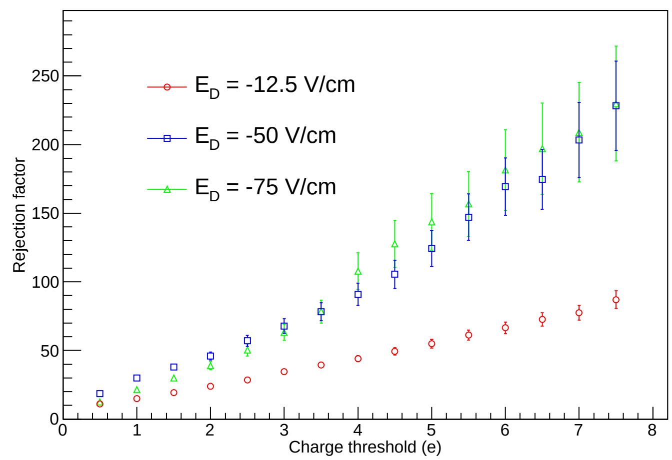

Fig. 56: Hadron rejection factor as a function of the amplitude threshold in units of the primary charge. The error bars represents the statistical uncertainties.

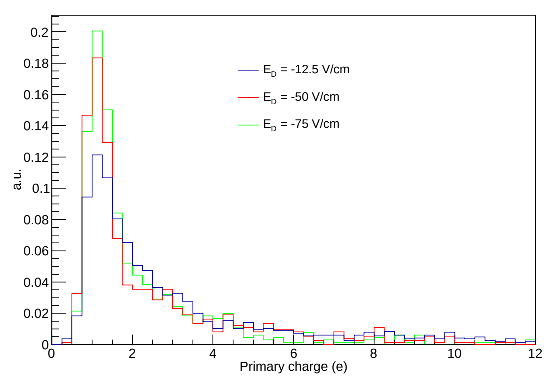

Fig. 57: Pulse-height spectra measured with pions at various values of the drift field E_{D}.

To achieve better hadron rejection factor, we increase the applied voltage across the top GEM (V_{GEM}) from 500 V to 520 V. As a result, the gain of the top GEM increases ~1.5 times. The final results of hadron rejection factor is shown in Fig. 58. The hadron rejection factor of $V_{\mathrm{GEM}} = 520$ V is larger than $V_{\mathrm{GEM}} = 500$ V at the same amplitude threshold since the very high gain of the top GEM can reduce the relative amount of the ionization charge produced in the transfer gap. We achieve the hadron rejection factor of 100 with electron detection efficiency of 70 %.

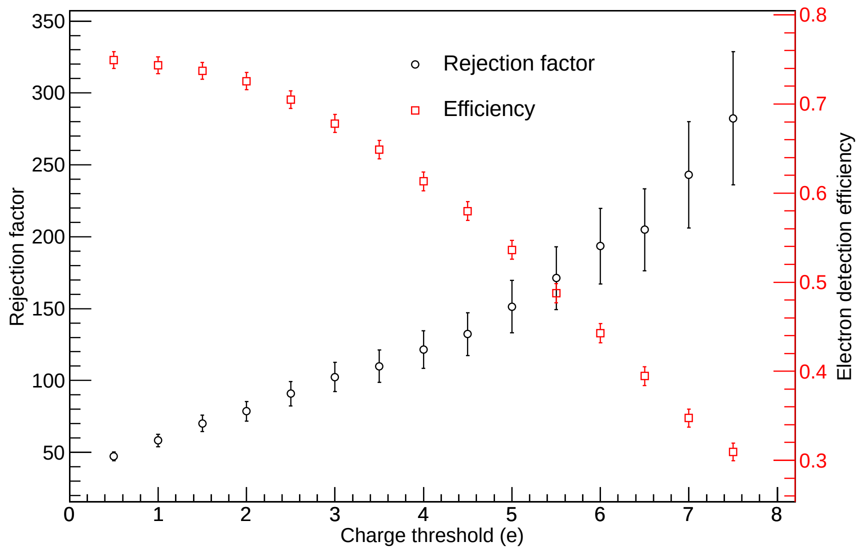

Fig. 58: Hadron rejection factor and electron detection efficiency derived from the pion and electron pulse-height distribution at $E_{\mathrm{D}} = -75$ V/cm as a function of the signal amplitude threshold in units of the primary charge. The applied voltage across the top GEM is 520 V.

8.10 Summary of T47

- We observe $\sim$7 photoelectrons and this value is smaller than we expected. We can estimate the transport efficiency of the Raytech-A from this results and it gives a value of 25 %.

- The optimum operation point is $E_{\mathrm{D}} = -75$ V/cm.

- The relative amount of the ionization charge produced in the transfer gap can be largely suppressed with high gain of the top GEM. This effect is reflected on the hadron rejection factor as shown in Fig. 46 and 59 which is derived without cluster size analysis.

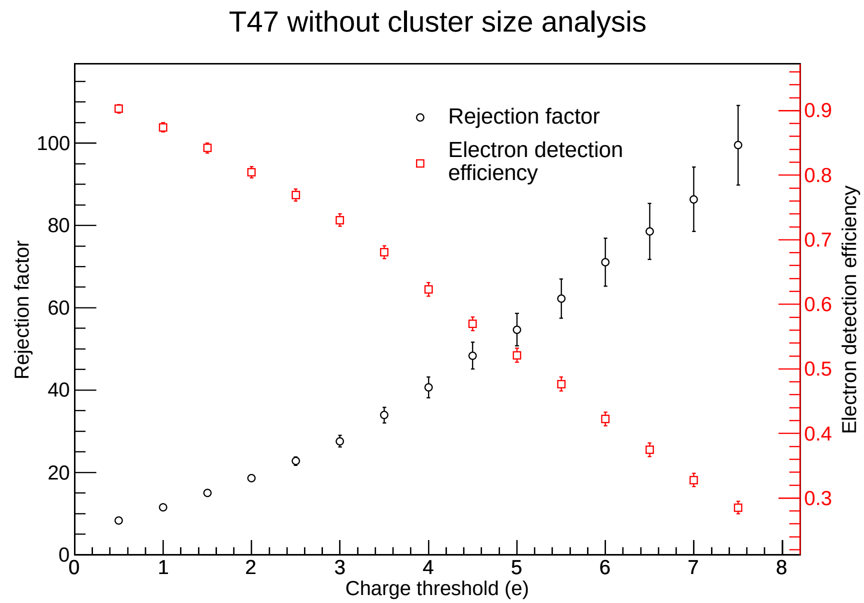

Fig. 59: Hadron rejection factor and electron detection efficiency derived from the pion and electron pulse-height distribution at $E_{\mathrm{D}} = -75$ V/cm without cluster size analysis as a function of the signal amplitude threshold in units of the primary charge. The applied voltage across the top GEM is 520 V.

The derived hadron rejection factor at the threshold of 5 e is 3 in Fig. 46 and 55 in Fig. 59. This improvement is due to decreasing of the relative amount of the ionization charge produced in the transfer gap. The gain of the top GEM is ∼7 in Fig. 46 and ∼50 in Fig. 59. An additional powerful hadron rejection factor with cluster size analysis can be seen in Fig. 58 and 59. Cluster size analysis increases the hadron rejection factor by ∼3 times.

- We achieve the hadron rejection factor of 100 with electron detection efficiency of 70 %.

9 Conclusion

The E16 experiment measures precise mass spectra of light vector mesons in nuclei with high statistics to investigate a partial restoration of the chiral symmetry at finite density. In E16 experiment, light vector mesons are generated by 30-GeV protons in target nucleus. Mass spectra are reconstructed by using a $e^{+}e^{-}$ pair decay channel since this decay channel is not affected by final state interactions. However, branching ratio of this channel is very small ($\sim 10^{-5}$). Furthermore, we have to use thin target ($\sim$0.1% interaction length and $\sim$0.3% radiation length) to reduce radiation tails on mass spectra and electron background from γ conversion in target materials. To overcome such small branching ratio and small interaction rate, we have to use high intensity primary proton beam of which intensity is 10^{10} proton per spill. To cope with 10^{7} Hz of interaction rate, we have to construct a new spectrometer using new technologies. The proposed spectrometer is based on design concepts of high rate capability and large acceptance. It consists of tracking device, gas Čerenkov counter and Lead Glass counter as shown in Fig. 7.

The tracking device consists of 3 layers of Gas Electron Multiplier (GEM) trackers. Particle momentum is determined by the GEM trackers. The GEM trackers are working up to 25 kHz/mm^2 in the COMPASS experiment while the highest counting rate in the E16 experiment is 5 kHz/mm^2. The required momentum resolution is 5 MeV which corresponds to the spacial resolution of 100 μm. Gas Čerenkov counter and Lead Glass counter serves as electron ID counter. Having large acceptance in limited volume, we use Hadron Blind Detector (HBD) as a gas Čerenkov counter. The HBD was originally developed for the PHENIX experiment at RHIC. The HBD is a mirror-less and window-less gas Čerenkov detector operated with pure CF_4. It has a 50 cm radiator directly coupled to a readout element consisting of a triple GEM stack, with CsI photocathode evaporated on the top surface of the top GEM and pad readout at the bottom of the stack. A hadron rejection factor of 100 with an electron detection efficiency of 70% is required for our experiment. Lead Glass counter is used as EM Calorimeter. The Lead Glass counter are used for additional electron ID and a hadron rejection factor of 25 is required. This thesis gives an account of the development and performance of the HBD for the E16 experiment.

Operation principle of the HBD is shown in Fig. 9. To accomplish good separation of electron and hadron, large number of photoelectrons which is produced by Čerenkov photon of incident electrons and minimization of signal strength for hadrons are important. To minimize signal strength of hadrons, ionization electrons produced in drift gap should not be collected while photoelectrons should be pulled into holes of the top GEM. Two methods can be considered to increase the number of photoelectrons pulled into holes of the top GEM, (1) making a CsI photocathode of high quantum efficiency. As quantum efficiency increases, the number of photoelectrons increases and effect of ionization electrons decreases. (2) increasing collection efficiency of photoelectrons.

Thus, we perform R&D of CsI photocathode and systematic measurement about collection efficiency of photoelectrons in the laboratory. GEM foils are made photosensitive by the vacuum evaporation of a thin layer of CsI on the GEM electrode surface. However, process of the evaporation and handling of the photocathode is not clear. We optimize such evaporation process and handling process by making a CsI photocathode in our laboratory. Fig. 27 shows quantum efficiency of our CsI photocathode and our photocathode achieve the best performance until the present.

Photoelectron collection efficiency of the CsI photocathode is also important. Photoelectrons produced on the surface of the CsI photocathode are not always pulled into holes of the top GEM. To investigate the various parameters affecting the photoelectron collection efficiency, we perform systematic measurements of collection efficiency. We measure collection efficiency of 3 different GEMs which differ hole diameter and thickness of insulating foil as shown in Table 6. The collection efficiency may depend on the electric field at the surface of photocathode and these GEMs have different electric field. Obtained collection efficiency of these GEMs is shown in Fig. 37. As a result, no difference between GEMs exists.

In addition, minimization of collection of ionization electrons in transfer gap is also important. The minimization of the collection of ionization electrons generated in the transfer gap is mainly achieved by high amplification of the top GEM, when the photoelectrons are sufficiently amplified by the top GEM, ionization electrons produced in the transfer gap which don't experience top GEM amplification are negligible compared with the amplified photoelectrons. By combining the results we obtained in laboratory test, we can estimate the number of photoelectrons we observe in beam test (equivalently, the E16 experiment). We can expect $\sim$15 photoelectrons in a beam test.

Based on the results of laboratory test, we constructed a prototype HBD for the E16 experiment. To evaluate a hadron rejection factor and electron detection efficiency, we perform beam tests two times at J-PARC K1.1BR beam-line. In the first test, we observe 12 photoelectrons while the expected value from laboratory results is 13.5 ± 1.0 photoelectrons. There is no contradiction in the number of photoelectrons and it indicates that the results of laboratory test and analysis of the beam test is valid. However, a hadron rejection factor of 10 and an electron detection efficiency of 35% are obtained. This results is not satisfactory for the E16 experiment and this is due to very low gain of the top GEM. To overcome the results of the first test, we improve GEMs and pad readout. (1) we produce new GEMs as shown in Table 10. The hole diameter of new GEMs is smaller than the GEMs used in the first test and it shows high gain. Furthermore, By using Raytech-A (see Table 10) as the top GEM we can expect more photoelectrons, since the effective area increase by $\sim$15%. (2) we use new pad readout for cluster size analysis. The readout pad in the first test consists of hexagonal pad and the side length of the hexagonal pads is 17 mm while the readout pad in the second test consists of square pads and the side length of the square pads is 10 mm. The first pad size is comparable to the Čerenkov blob size (radius of 17 mm) to obtain maximum signal-to-noise ratio, however in the second test we can obtain enough signal-to-noise ratio due to high gain even if a pad detects part of Čerenkov light. Pions produce a signal on single pad since ionized electrons are localized along the track whereas electrons most probably produce multiple-pad hits due to Čerenkov blob. Thus we can obtain additional hadron rejection power with cluster size analysis.

We observe 7 photoelectrons in the second test. This may be caused by the lower collection efficiency between produced photoelectrons and hole of top GEM. However, a hadron rejection factor achieved in the second test is almost 100. This is due to high gain of the top GEM and finer segmentation of readout pads. The high gain of the top GEM contributes in two aspects. One is a good signal-to-noise ratio. We can perform cluster size analysis due to good signal-to-noise ratio. The other is a suppression of contributions of ionization charge generated in the transfer gap.

Relative amounts of ionization charge produced in the transfer gap is reduced by high gain of the top GEM. Finally, We achieve a hadron rejection factor of 100 with an electron detection efficiency of 70 % in the second test with cluster size analysis.
These values satisfy the requirement of the E16 experiment. We succeed in developing the HBD for the E16 experiment.

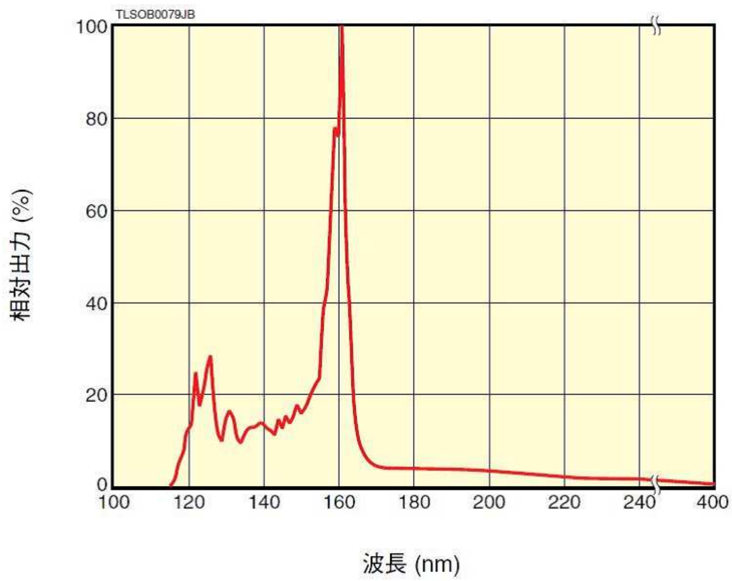

Fig. 60: Relative intensity of deuterium lamp as a function of wavelength.

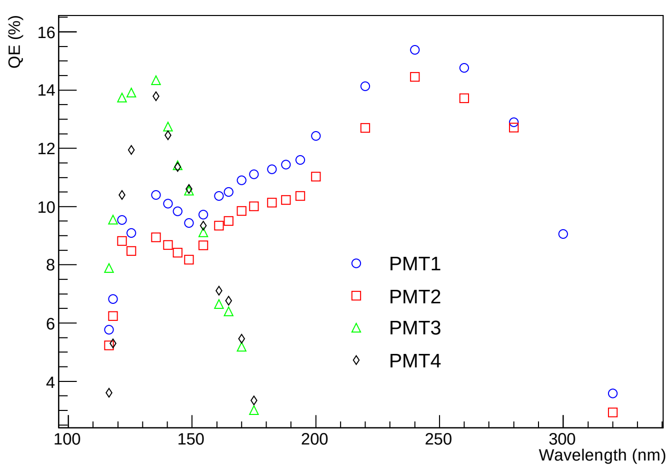

Fig. 61: QE of the PMTs.

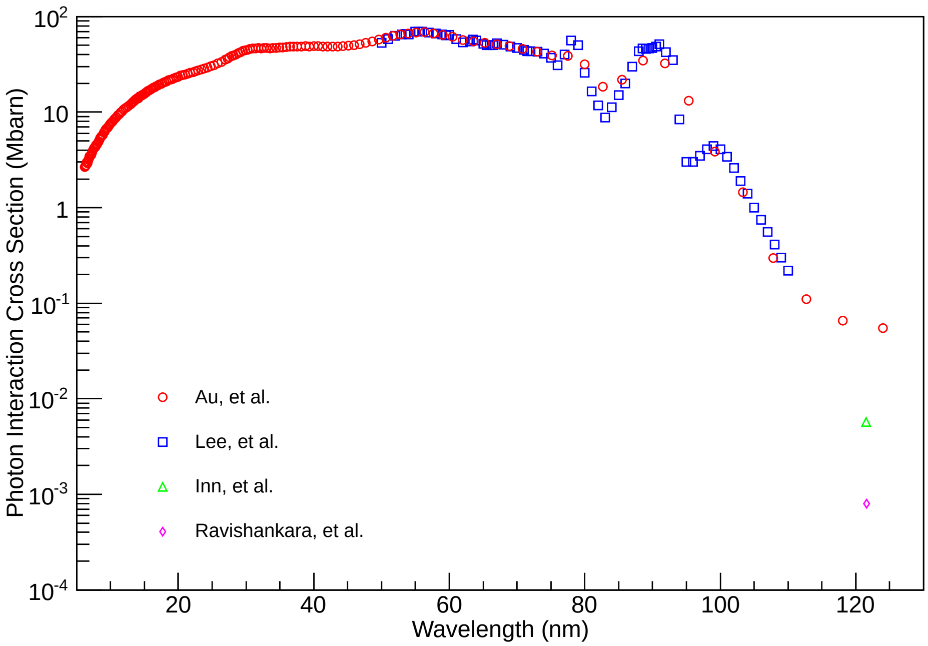

Fig. 62: Photon absorption cross section as a function of wavelength [29–32].

References

[1] D.J. Gross and F. Wilczek, Phys. Rev. Lett, 30 (26) 1343-1346

[2] S. Bethke, Prog. Par. Nucl. Phys. 58 (2007) 351-386

[3] K.G. Wilson, Phys. Rev. D 10, 2445-2459 (1954)

[4] Y. Nambu and G. Jona-Lasinio, Phys. Rev. 122, 345-358 (1961)

[5] Y. Nambu and G. Jona-Lasinio, Phys. Rev. 124, 246-354 (1961)

[6] T. Hatsuda and S.H. Lee, Phys. Rev. C 46 (1992) 34

[7] F. Klingl, N. Kaiser, and W. Weise, Nucl. Phys. A624 (1997) 527

[8] G.E.Brown and M.Rho, Phys. Rev. Lett. 66 (1991) 2720

[9] D. Adamova et al., Phys. Lett. B 666 (2008) 425

[10] S. Damjanovic, Nucl. Phys. A 783 (2007) 327-334

[11] R. Muto et al., Phys. Rev. Lett. 98 (2007) 042501

[12] M. Naruki et al., Phys. Rev. Lett. 96 (2006) 092301

[13] M.H.Wood, Phys. Rev. C 78 (2008) 015201

[14] D.Trnka et al, Phys. Rev. Lett 94 (2005) 192303

[15] F. Sauli, Nucl. Instr. and Meth. A 386 (1997) 531

[16] B. Ketzer, Q. Weitzel, S. Sauli and L. Ropelewski, Nucl. Instr. and Meth. A 535 (2004) 314

[17] W. Anderson, et al., Nucl. Instr. and Meth. A 646 (2011) 35-58

[18] R. Abjean, A. Bideau-Mehu and Y. Guern, Nucl. Instr. and Meth. A292 (1990) 593-594

[19] G. Malamud et al., Nucl. Instr. and Meth. A 335 (1993) 136-145

[20] A. Breskin, Nucl. Instr. and Meth. A 371 (1996) 116-136

[21] K. Watanabe and M. Zelikoff, J. Opt. Soc. Am. 43 (1953) 753

[22] K. Yoshino, J.R. Esmond, W.H. Parkinson, K. Ito and T.Matsui, J. Chem. Phys. 211 (1996) 387

[23] K. Yoshino, W.H. Parkinson, K. Ito and T.Matsui, J. Molec. Spec. 229 (2005) 238-243

[24] J. Seguinot et al. Nucl. Instr. and Meth. A 297 (1990) 133

[25] R. Gernhauser et al., Nucl. Instr. and Meth. Phys. Res. A 371 (1996) 300-304

[26] B. Azmoun, et al., IEEE Trans. Nucl. Sci. NS-56-3 (2009) 1544-1549

[27] B. Azmoun, et al., IEEE Trans. Nucl. Sci. NS-57-4 (2010) 2376-2381

[28] J. Va'vra et al., Nucl. Instr. and Meth. A 324 (1993) 113-126

[29] Jennifer W. Au, Gordon R. Burton and C.E. Brion, Chem. Phys. 221 (1997) 151-168

[30] L.C. Lee, Xiuyan Wang, and Masako Suto, J. Chem. Phys. 85, 6294 (1986)

[31] E.C.Y. Inn, J. Geophys. Res. 85, 7493-7494 (1980)

[32] A.R. Ravishankara, S. Solomon, A.A. Turnipseed, and R.F. Warren, Science 259, 194-199 (1993).